JOURNAL OF MATERIALS RESEARCH AND TECHNOLOGY 2023;24:8735–8753

Available online at www.sciencedirect.com

jmr&t Journal of Materials Research and Technology

journal homepage: www.elsevier.com/locate/jmrt

Improving mechanical properties and antibacterial response of α/β ternary Ti–Ta alloy foams for biomedical uses

C. Aguilar [a],**, F. San Martín [a], C. Martínez [b], B. Cámara [c], F. Claverías [c], A. Undabarrena [c], M. Sancy [d], V. Salinas [e], L. Muñoz [f],*

[a] Departamento de Ingeniería Metalúrgica y de Materiales, Universidad Técnica Federico Santa María, Av. España 1680, Valparaíso, Chile
[b] Departamento de Ingeniería en Obras Civiles, Universidad de La Frontera, Francisco Salazar, Temuco, 01145, Chile
[c] Departamento de Química y Centro de Biotecnología Daniel Alkalay Lewitt, Universidad Técnica Federico Santa María, Av. España 1680, Chile
[d] Escuela de Construcción Civil, Facultad de Ingeniería y Centro de Investigación en Nanotecnología y Materiales Avanzados "CIEN-UC", Pontificia Universidad Católica de Chile, Av. Vicuña Mackenna 4860, Macul, Santiago, Chile
[e] Instituto de Ciencias Químicas Aplicadas, Facultad de Ingeniería, Universidad Autónoma de Chile, Av. Pedro de Valdivia 425, Providencia, Santiago, Chile
[f] Instituto de Química, Facultad de Ciencias, Pontificia Universidad Católica de Valparaíso, Avda. Universidad 330, Placilla (Curauma), Valparaíso, Chile

ARTICLE INFO

Article history:
Received 19 March 2023
Accepted 11 May 2023
Available online 16 May 2023

Keywords:
Hardness
X-ray analysis
Titanium alloys
Powder methods

ABSTRACT

This study investigates the potential of Ti–Ta–Sn alloys for biomedical applications due to their excellent mechanical properties and biocompatibility, with a particular focus on their use in trabecular bone replacement. This work aims to analyze the influence that of Sn has on the mechanical properties and antibacterial response of α–β ternary Ti–13Ta–xSn (x:3, 6, 9, and 12 at.%) alloy foams. The Ti-based alloys were designed considering three aspects; (i) final microstructure, (ii) alloying element types, and (iii) thermodynamics while using MAAT and ThermoCalc software. The alloys were obtained by mechanical alloying, with used milling times being 30 h for Ti–13Ta–3Sn, 10 h for Ti–13Ta–6Sn, 10 h for Ti–13Ta–9Sn, and 15 h for Ti–13Ta–12Sn. The foams were obtained using NaCl as the space holder (50 v/v% porosity) and consolidated by a hot pressing method at 780 °C for 30 min, applying a load of 40 MPa. Both the *Staphylococcus aureus* ATCC 6538 strain and *Escherichia coli* ATCC 8739 strain were used to evaluate the antibacterial responses of Ti-based alloy foams. The Ti-based alloy foams were composed mostly by a mix of α and β-phases. The metallic foams exhibited relative homogeneous pore distribution with a size between 100 and 450 μm and having an average porosity slightly higher than 50%. The samples showed elastic modulus values between 1 and 2 GPa, compressive yield strengths over 150 MPa, and microhardness over 450 HV. All Ti-based alloy foams showed no antibacterial activity nor bacterial adhesion, indicating that there is bacterial adhesion inhibition.

---

* Corresponding author.
** Corresponding author.

E-mail addresses: claudio.aguilar@usm.cl (C. Aguilar), lisa.munoz@pucv.cl (L. Muñoz).

https://doi.org/10.1016/j.jmrt.2023.05.115

1. Introduction

Titanium and its alloys are widely used in scientific and technological applications in various areas such as; aerospace, nuclear, car, marine, and biomedical, due to their high strength to weight ratio, relative lower density, excellent corrosion resistance [1–3], and biocompatibility with the human body [4]. In the aerospace field, Boeing and Airbus companies forecasted that the use of Ti-based alloys per plane is expected to increase in the coming years due to their high resistance to creep and oxidation, good formability, and favorable strength/density ratio [5]. In the nuclear industry, Ti-based alloys are used as a beam window materials [6]. In the car industry, Ti-based alloys are used for fabricating connecting rods, valves, wheel rim screws, and suspension springs for racecars [3], whereas, in marine industries, these alloys are used in desalination plants, as well as cooling systems in seawater-cooled power plants [3]. Titanium and Titanium alloys are widely used in medical devices because they meet several criteria due to their mechanical properties, corrosion resistance, and biocompatibility [7–11]. In dental implants, the most commonly used materials are commercially pure (cp) Ti (grade 2 and grade 4) and Ti–6Al–4V alloy that undergo a surface treatment to optimize contact between bone cells and the device [12]. The disadvantages of cp-Ti for biomedical applications include a higher elastic modulus, relatively low mechanical strength, and low wear resistance [13]. Also, Ti–6Al–4V alloys are used as orthopedic replacements due to their noteworthy combination of mechanical properties (strength and ductility) [14]. The main disadvantages of an Ti–6Al–4V alloy are, (i) Al and V ions can be released into the human body [15,16], which could contribute in loosening of hip, knee prostheses and increases the probability of diseases such as dermatitis, Alzheimer, neuropathy, and osteomalacia [17,18] and damage to the nervous system [19,20], and (ii) the elastic modulus is larger than that of the human bone, producing a stress-shielding effect [21]. This effect is attributed to the fact that the metal implant supports a disproportionate part of the load compared to the load supported by the bone [22]. As consequence, a stiffness mismatch between the implant materials and human bones causes bone resorption and eventually loosening of the implants.

Regarding the first disadvantage, Ti-based alloys with non-toxic elements, such as Nb, Mo, Zr, Sn, or Ta have been explored [23–25]. Ti-based alloys focusing on the formation of the β-Ti-based alloy, with Nb, Mo, Zr, Ta, and Sn elements have shown many advantages for orthopedic implant applications, including excellent biocompatibility and having a high resistance to biological corrosion [26–28]. These alloys have an elastic modulus ranging between 50 and 100 GPa [1,11,29–31], which is lower than the elastic modulus of a Ti–6Al–4V alloy (112 GPa [11]), yet still high when compared to that of bone structures (3–30 GPa) when considering the type and anisotropy of human bones [32–35].

Regarding the second disadvantage mentioned above, the stress shielding effect, possible alternatives to change the elastic modulus are; i) the formation of a solid solution [36,37], ii) synthesis of composite materials [38,39], or iii) synthesis of metallic foams [21,25,40]. The latter alternative has been explored to tailoring the elastic modulus of Ti-based alloys for human bone requirements. This minimizes or eliminates stress shielding, increases the probability of the new bone growth, and eventually prolongs the life of the implant [41–44].

Pure Ti, along with a great number of its alloys, exhibits a phase change at the β-transus temperature. At temperatures below the β-transus, Ti exhibits a hexagonal close-packed (hcp) crystalline structure (called α-phase), while above this temperature possessing a body-centered cubic (bcc) crystalline structure (called β-phase). In addition to these phases, metastable face-centered-cubic (fcc or γ-phase) structures have been reported [45–47]. Two specific conditions are required to form γ-phase, high deformation, and nanocrystalline grains size. Both conditions are achieved during milling process.

Ta and Sn are biocompatible elements due to them exhibiting negligible effects on the human body [4]. β-binary Ti–Ta-based alloys have attracted great interest due to their excellent combination of having high strength, a relatively low modulus, and corrosion resistance that is superior to that of pure Ti [48]. Ta is a strong β-stabilizer in Ti-based alloys because it decreases the β-transus from 882 up to ~500 °C at 50 at.% [49,50] and Sn slightly influences the β-transus [51], such as when at 5 at.% Sn, the β-transus temperature decreases from 882 up to 841 °C. From a biomedical applications point of view, β-Ti-based alloys are preferable, exhibiting a smaller elastic modulus than α-Ti-based alloys, thus reducing the stress-shielding effect. In addition, β-Ti-based alloys exhibit an elastic modulus which is closer to that of human bone [11]. The main benefits of using Ta and Sn as alloying elements in Ti-based alloys are: (1) the cost of Sn is less in comparison to other alloying elements, (2) Ta and Sn are considered highly biocompatible [4], (3) Ta and Sn exhibit antibacterial activity against different pathogens [52,53], such as *Staphylococcus aureus* and *Escherichia coli* [54,55] and (4) Ta decreases the modulus of elasticity of Ti-based alloy without decreasing the strength [56].

A disadvantage of adding porosity to Ti-based alloys could be a decrease in corrosion resistance, as previously reported [57–60], although Guerra et al. [21] recently reported that the passivity behavior of a Ti–Nb–Ta–Fe–Mn alloy was not influenced by the introduction of porosity after 90 days of exposure to Hank's solution. It is worthy to mention that the presence of microorganisms can also determine the corrosion resistance of Ti-based alloys due to the adhesion of bacteria and subsequently biofilm formation [61,62], triggering local chemical composition at the interface oxide/media. Infected implants usually require revision surgery, becoming one of the most devastating and costly complications since it involves longer hospital stays, significantly high costs for patients, and higher mortality rates [63,64]. The genus *Staphylococcus* causes the largest number of infections on patients with implants, approximately 4 in 5 cases, with *S. aureus* and *Staphylococcus epidermidis being* the predominant species in the number of infections (2 in 3 cases) [65]. In particular, *Staphylococcus* is a Gram-positive, aerobic, and facultative anaerobic microorganism [66] whose cells are spherical shaped and have a diameter between 0.5 and 1 μm [67]. Recently, Silva et al. [68] reported that the composition of the oxide layer formed on a Ti–6Al–4V was drastically influenced by the added porosity and the presence of *S. aureus* in Hank's solution. Pruchova et al. [8] studied a nanostructured surface of a TiAlV alloy that contained silver deposits, obtaining an antimicrobial surface against *S. aureus* as well as *E. coli*. This bacterium is a Gram-negative bacterium that belongs to the Enterobacteriaceae family [66]. These bacteria are rod-shaped and facultative anaerobes which are found in the human gut, making them the most abundant facultative anaerobe in the intestinal microbiota [69]. Microorganisms belonging to the *Staphylococcus* genus are the ones that cause most infections in medical implants. It has been found that *E. coli* contributes to between 20 and 30% of medical implant related infections [65,66].

Based on the information presented, this study aims to analyze the influence of two microorganisms (*E. coli* and *S. aureus*) and the amount of Sn on the antibacterial response and mechanical properties of α/β-ternary Ti-based alloys (Ti–13Ta-xSn, x:3, 6, 9 and 12 at.%). The powder metallurgy approach was used to obtain metallic foams and the amount of Sn was chosen based on thermodynamic analysis to promote the presence of hcp (α-phase) and bcc solid solution (β-phase) after the consolidation process.

2. Materials and methods

2.1. *Metallurgical design of alloys*

In this work, a α/β-ternary Ti-based alloy (Ti–13Ta–xSn, x:3, 6, 9, and 12 at.%) was selected according to the following criteria.

(a) **Microstructure**: A microstructure composed of a mix of α and β-phases must be obtained after a consolidation process.

(b) **Alloying elements**: The amount of Ta (13 at.%) in the Ti-based alloys was chosen based on its effect on the mechanical properties of Ti-based alloys, (i) achieving a smaller elastic modulus by adding approximately 10 at.% Ta [70] and (ii) obtaining a higher tensile strength between 10 and 20 at.% [11]. The addition of 13 at.%Ta provides a good combination of high strength and low elastic modulus [11] but when the addition of Ta is increased beyond at.%13, the density of the alloy significantly increases, which is unfavorable for biomedical applications [11,71]. A low amount of Sn was chosen to decrease the possibility of forming liquid during sintering.

(c) **Thermodynamics analysis**: The Ti–Ta–Sn system was thermodynamically analyzed using the Materials Analysis Applied Thermodynamic (MAAT) [72] and ThermoCalc softwares. Fig. 1a and b shows the Gibbs free energy of mixing (ΔG^{M}) and the ideal Gibbs free of mixing ($\Delta G^{M,id}$) to form solid solutions in the Ti–Ta–Sn ternary system at any given composition at 25 °C obtained using the MAAT. The ΔG^{m} values are negative and smaller than $\Delta G^{M,id}$ values in the whole composition range, suggesting that there is a driving force to form a solid solution from elemental Ti, Ta and Sn powders. The semicircles of dotted lines in the three corns show that solid solutions are not formed due to $\Delta G^{M} \geq \Delta G^{M,id}$. Fig. 1c shows the calculated Ti–Ta–Sn phase diagram at 780 °C using ThermoCalc software. It is possible to observe that compositions used in this study meets the microstructure requirements (α/β phases).

There are considerable differences between melting temperatures and densities of Ti, Ta, and Sn, making it challenging to obtain this ternary alloy using traditional melting and casting methods As a result, metallic foams of Ti-based alloys were obtained through a powder metallurgy technique, using the space-holder method for synthesizing foams.

2.2. *Mechanical alloying*

The elemental powders of Ti (99.5%, −149 μm, NAOH Tech. Co.), Ta (99.9%, −44 μm, Sigma–Aldrich) and Sn (99.5%, <150 μm, Sigma–Aldrich) were used to synthesize Ti–13Ta-xSn (x:3, 6, 9, and 12 at.%) alloys. A 2 wt. % stearic acid ($C_{18}H_{35}O_2$, 99%, Loba Chemie) was used as a process control agent. The alloys were milled using a Retsch PM400 planetary mill at 250 rpm, using vials and balls of Ytria Stabilized Zirconia (YSZ) under an ultra-pure Ar atmosphere (>99.999%Ar, $O_2 \leq 1.0$ ppm, $H_2O \leq 1$ ppm, $CO_2 \leq 1$ ppm, $N_2 \leq 4.0$ ppm and total hydrocarbons ≤0.5 ppm). Balls 5 mm and 10 mm in diameter (1:1 ball ratio) and the ball/powder ratio of 10:1 were used. Jar and balls of YSZ were used since that during milling powders are contaminated by the materials from the Jar and balls. The presence of YSZ in Ti-based alloy milled powders is beneficial because it enhances the biocompatibility of the foams [73,74]. The milling time for each alloy was chosen to maximize the quantity of the β-phase. The experimental study of the effect of the milling time on the evolution of phases was made previously by our group [75]. The milling times used were 30 h for Ti–13Ta–3Sn, 10 h for Ti–13Ta–6Sn, 10 h for Ti–13Ta–9Sn, and 15 h for Ti–13Ta–12Sn. The milling was carried out at room temperature with an on/off cycle of 30 min each to keep the temperature constant.

2.3. *Consolidation of foams*

The synthesis of metallic foams was done using the spacer-holder method. Milled Ti–Ta–Sn powders were mixed with 50 v/v% NaCl particles with particle sizes ranging between 200 and 400 μm. Milled powder and NaCl particles were mixed in a mixer mill RETSCH model MM 400 for 45 min at a frequency of 30 Hz. Green samples with 8 mm in diameter and 3 mm in height were obtained in hardened steel die, applying a load of 550 MPa for 90 s, with hot pressing (HP) being carried out on an 8 mm diameter graphite matrix afterwards. The thermal cycle consisted of three steps at (i) 300 °C for 5 min, (ii) 600 °C for 5 min, and (iii) 780 °C for 30 min at a load of 40 MPa. The maximal temperature of 780 °C was used to avoid NaCl being melted. A flow of ultra-pure Ar was used as an atmosphere during the sintering process, 5 L $\min^{-1}$ for 30 s at 20 °C to remove the air within the chamber and 1 L $\min^{-1}$ during the rest of the process. After sintering, NaCl particles were

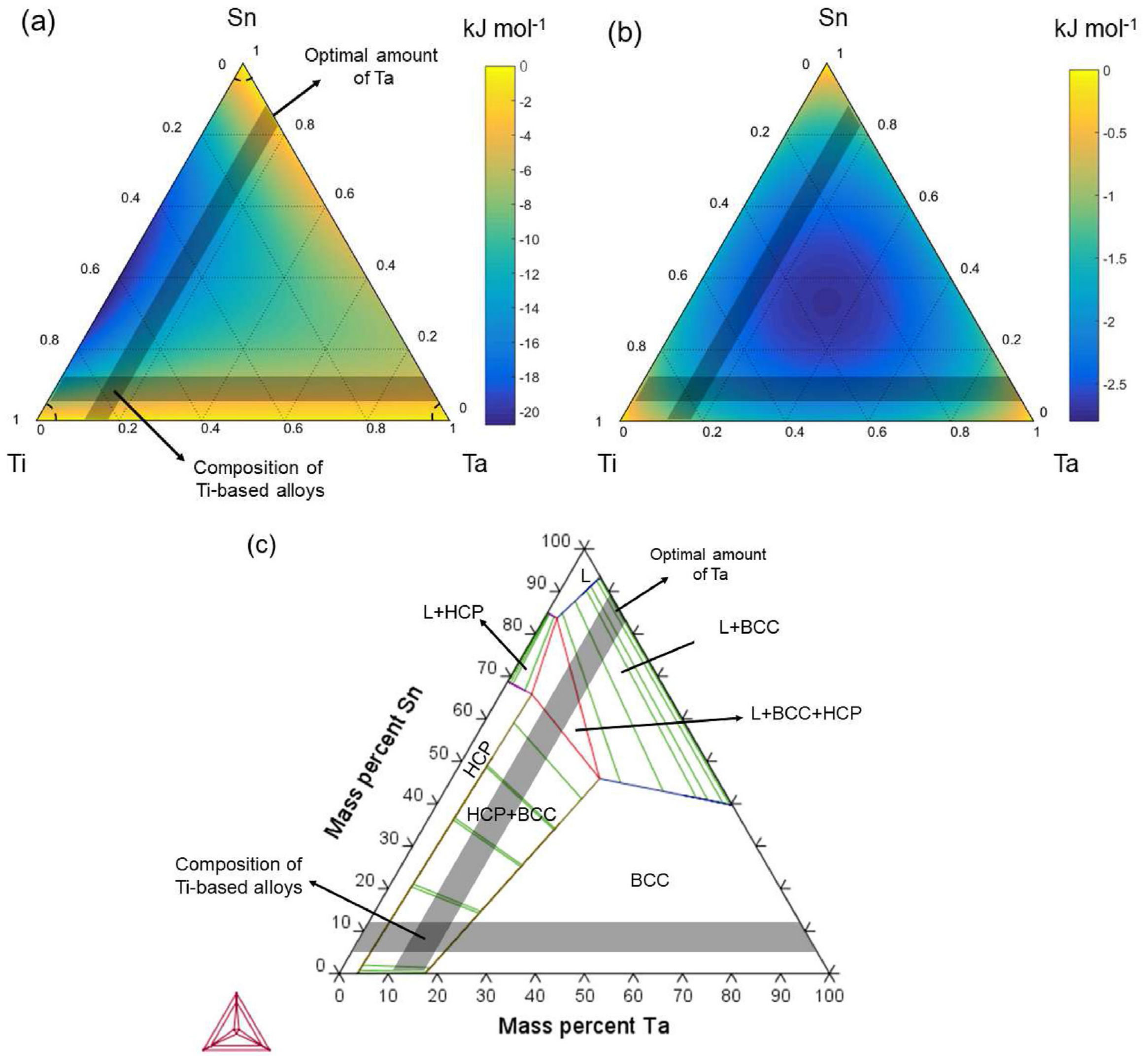

Fig. 1 – (a) Ternary diagram of Gibbs free energy of mixing of Ti–Ta. Sn system at 25 °C and (b) ideal Gibbs free energy of mixing at 25 °C and (c) calculated ternary Ti–Ta–Sn phase diagram at 780 °C using ThermoCalc software.

removed via the dissolution technique in sequential cycles. Each cycle consisted of immersing the samples in a bath of distilled water at 50 °C for 1 h, then samples being dried at 110 °C for 1 h in a furnace and subsequently weighted. The dissolution technique end when the difference in the mass of the sample was $\leq$0.01 g.

2.4. *Characterization of powders and foams*

The morphology of the powders was determined using a scanning electron microscope (SEM) model QUANTA FEG 250, and the elemental composition was determined using an EDAX brand detector model OCTANE PRO. The foam samples were mechanically polished with SiC paper of grades 240 to 1000, followed by a sequential diamond paste polish using three particle sizes (6, 1, and 0.25 μm) on a polishing cloth. Each polished sample was rinsed with distilled water and placed in an ultrasonic bath for 10 min before being dried in a desiccator at room temperature. The porosity of the foams was determined by image analysis in a Leica DM500 model microscope with the Leica Application Suite (LAS) software for image processing. The determination of the porosity (p), and the morphological parameters of the pores: equivalent diameter (D_{eq}), form factor (F_f), convexity (R), and pore density (D_p) were performed using the Image J software in order to do an image analysis. A cross-section of the foams was analyzed, and the statistical analysis of data was done using the OriginPro 9.1 software.

The X-ray diffraction (XRD) patterns were recorded using a STOESTADI MP equipped with a DECTRIS MYTHEN 1K detector and a Cu-$K_{\alpha 1}$ radiation ($\lambda = 0.15406$ nm). The XRD patterns were measured in an angular range of 2θ between 20° and 120°, with a step angle of 0.12° and a time for each step of 10 s.

The microstructural evolution was obtained from Rietveld refinements of the X-ray powder diffraction patterns using the Materials Analysis Using Diffraction (MAUD) software [76,77]. The LaB6 (a = 4.1565 (1) Å) was used as external standard for determining instrumental broadening [78]. To account for the

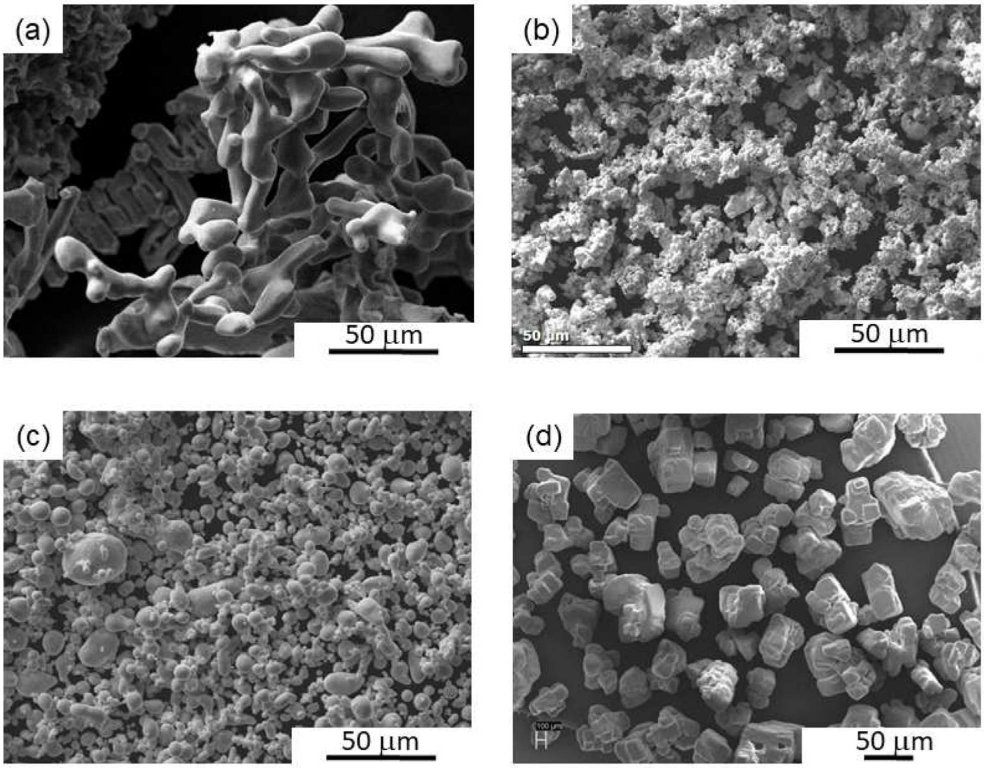

Fig. 2 – SEM images of elemental powders (a) Ti, (b) Ta, (c) Sn (500X) and (d) NaCl (57X).

microstructure analysis, the profile fitting was performed by considering the Delf line broadening model [79,80], an isotropic and anisotropic size-strain model, considering the Popa's rule [81] and texture [82].

Vickers microhardness was measured using the Lewick Zwick Roell Indentec microdurometer, DM500 model. A load of 50 g was applied for a time of 15 s with each indentation, in accordance with ASTM E384 [83]. The elastic modulus was obtained using the "pulse transmission" technique. The elastic modulus was obtained using an ultrasonic piezoelectric transducer contact Olympus, V156, and V110 transducers by using shear and longitudinal waves that were generated by Agilent 33220A equipment and subsequently amplified by NF BA4850 equipment (30 V and 1 MHz). Both emission and reception signals were acquired by the Tektronix TDS2012 oscilloscope, with a temporal sensitivity of 1 ns. The measurements were made according to ASTM D2845-08 [84]. The compression test to determine the yield strength was carried out based on the ISO 14317 standard [85] at a constant speed of 0.05 [mm/min] using a Zwick Roell Universal Testing Machines, Z030 model. To determine the macroporosity and density of the foams, the Archimedes principle was employed in accordance with the Standard Test Method ASTM C373-88.

2.5. *Antibacterial screening of foams*

The Gram-positive bacteria *S. aureus* ATCC 6538 and Gram-negative *E. coli* ATCC 8739 were used as test microorganisms. Previously, the foams were sterilized by autoclaving at 121 °C for 20 min, to ensure sterility. Test strains were initially grown on a solid agar LB culture medium (10 g/l tryptone, 5 g/l yeast extract, 10 g/l sodium chloride, 18 g agar, in 1000 mL of distilled water) and incubated at 37 °C overnight. Bacterial colonies were inoculated in a 5 mL LB broth medium (with no agar) and incubated at 37 °C for 18 h on a rotary shaker at 250 rpm. Next, te Soft-agar overlay technique was used to screen for antibacterial activity. Briefly, a LB medium with melted soft agar (0.7% agar) was added to 12-well plates. The sterile foams and 15 ul of bacterial suspension with a final OD_{600} of 0.1 were added to each well. The antibiotic streptomycin was used as a positive control at a concentration of 33 µg/mL and the strain without the foams was used as a negative control. Once the molten agar had solidified, it was incubated overnight at 37 °C. The observation of an inhibition zone corresponding to a halo or transparent zone, indicated that the strain showed no, nor reduced, growth, respectively.

3. Results and discussion

3.1. *Characterization of unmilled and milled powders*

It is convenient to perform a characterization of raw powders as it influences the milling process. Fig. 2 shows the morphology and size of elemental powders used in the mechanical alloying. Ti powder is shown an irregular and spongy morphology, Fig. 2a. There are some fiber-shaped particles with faceted planes due to industrial production process

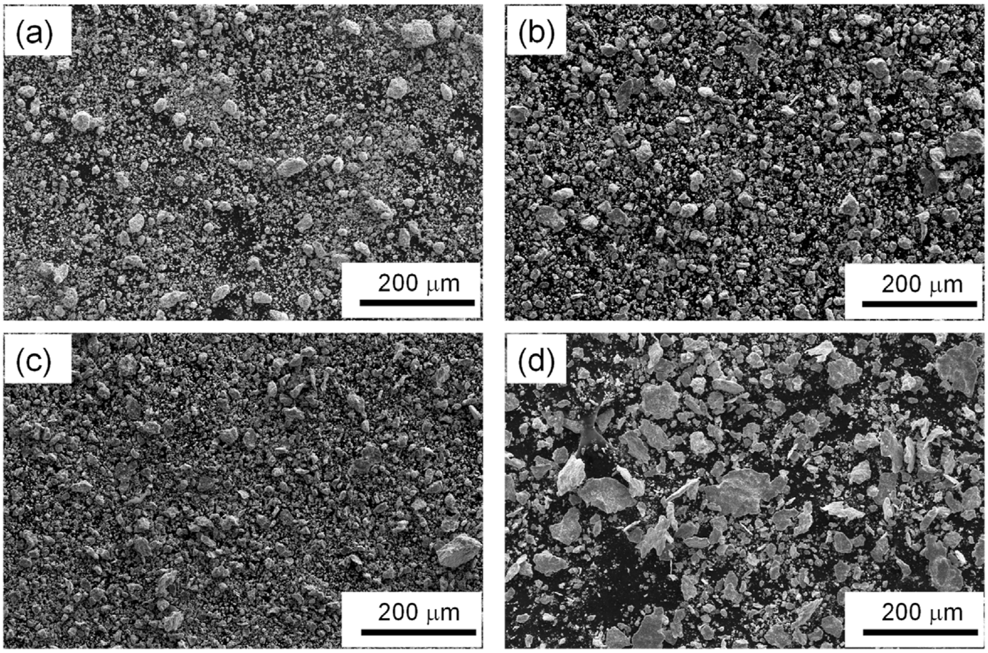

Fig. 3 – SEM images of alloys after milling, (a) Ti–13Ta–3Sn, (b) Ti–13Ta–6Sn, (c) (c) Ti–13Ta–9Sn and (d) Ti–13Ta–3Sn (500X).

characteristic for this element [86]. Ta powders exhibit with an irregular morphology and rounded edges and particle size smaller than 44 μm, Fig. 2b. These characteristics are typical of production by the method of reducing potassium heptafluorotantalate (K_2TaF_7) sodium salts [87]. Sn powders have a spherical morphology with powder size less than 45 μm, Fig. 2c. This morphology is typical of atomization processes, one of the most commonly used methods for producing of this element [88]. The XRD patterns that demonstrate the purity of these elemental powders are shown in supplementary

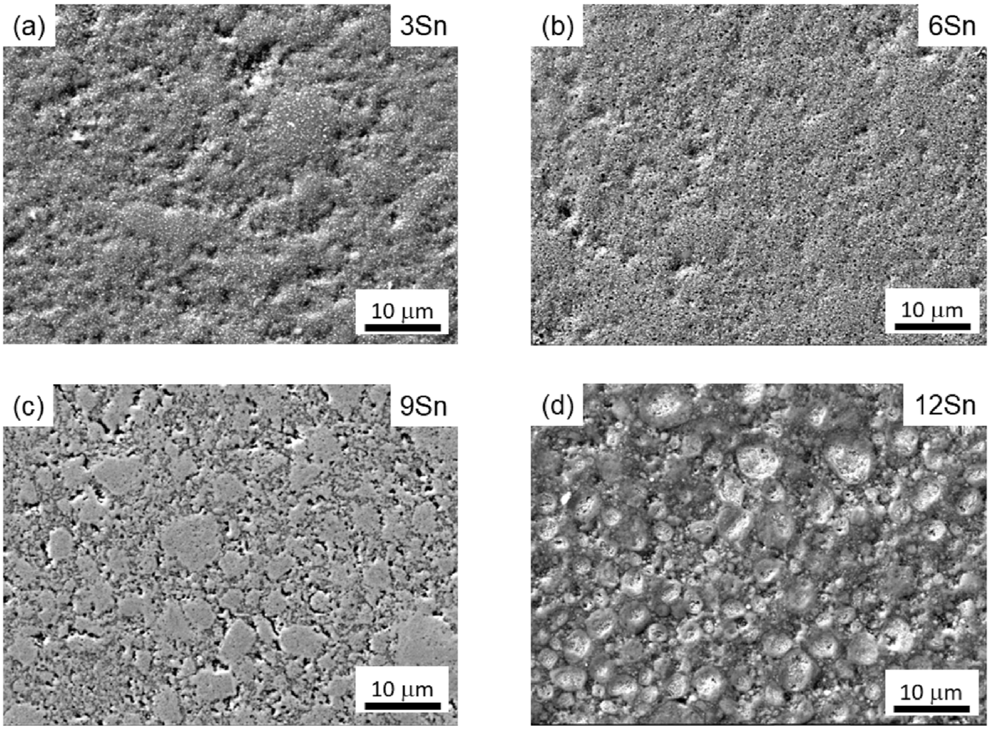

Fig. 4 – SEM images of microstructures of alloys, (a) Ti–13Ta–3Sn, (b) Ti–13Ta–6Sn, (c) (c) Ti–13Ta–9Sn and (d) Ti–13Ta–3Sn (2000X).

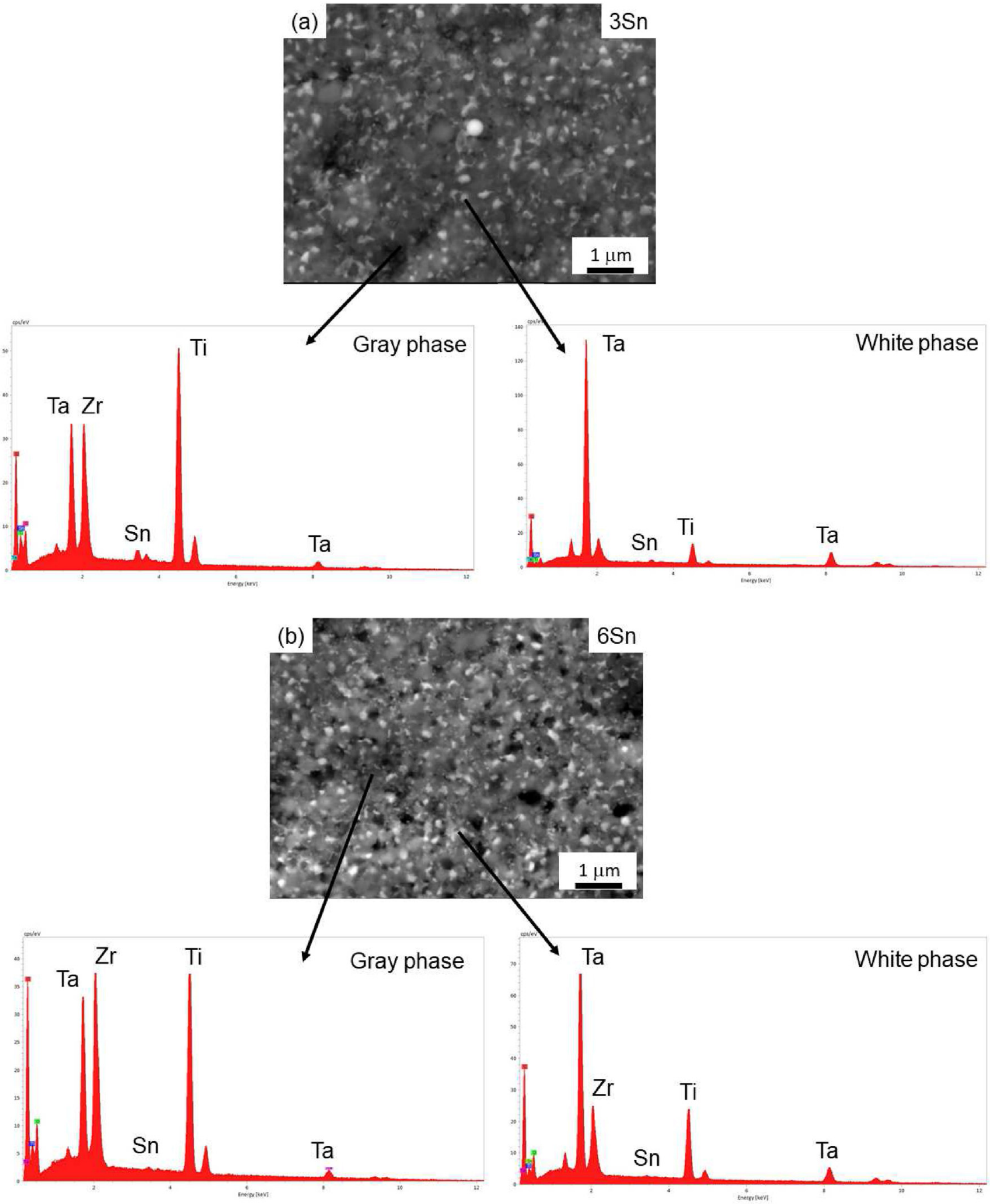

Fig. 5 – Microstructures and EDS analysis of (a) Ti–13Ta–3Sn and (b) Ti–13Ta–6Sn (15000X).

materials. Ti exhibits a hexagonal close-packed structure (HCP) with a P63/mmc spatial group characteristic of the α-Ti phase, Ta has a body-centered cubic structure (BCC) with a lm-3m space group, while Sn shows a tetragonal structure with a spatial group l141/amd typical of the β-Sn phase.

SEM images of Ti–Ta–Sn alloys after mechanical alloying are shown in Fig. 3. In general, an irregular morphology with rounded edges is observed for all alloys. The smallest particle size is for the Ti–13Ta–3Sn alloy and the biggest for the Ti–13Ta–12Sn alloy. A slight grade of agglomeration was observed of small particles on large particles. The agglomeration process occurs because the surface tension of the powders is modified by the amount of Sn and surface area during the mechanical alloying process. The driving force for the agglomeration of the powders is the increment of surface energy and tension [25]. The irregular morphology of particles shows the predominance of the fracture process over the cold-welding process.

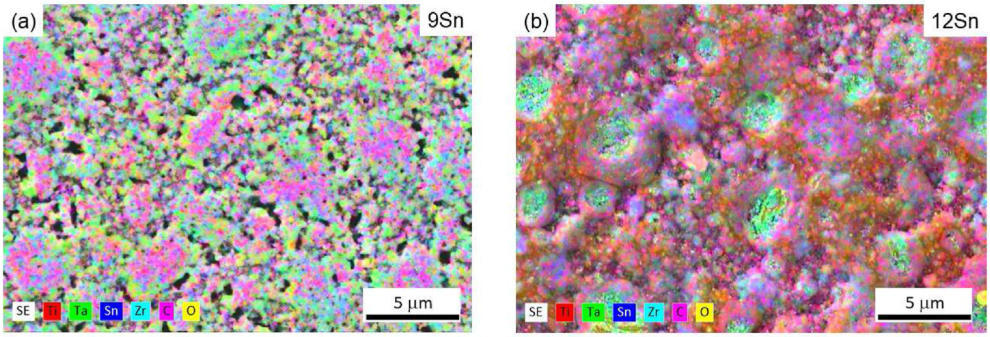

Fig. 6 – Microstructures and mapping-EDS analysis of (a) Ti–13Ta–9Sn and (b) Ti–13Ta–12Sn (5000X).

3.2. *Characterization of physical and mechanical properties of foams*

(a) Microstructures of foams

Fig. 4 shows SEM images where the microstructures of the bulk part of the foams of the four alloys are compared. The samples with 3 and 6Sn shows a similar microstructures composed of metallic matrix with a dispersion of small second phase particles, Fig. 4a and b. To this magnification (2000X) the microstructure is no resolved. The microstructure is resolved at a magnification of 15000 X, Fig. 5. It is noted the presence of two phases, a metallic matrix (gray) and small second phase particles (white) with sizes smaller than 500 nm. The EDS analysis shows that the second phase particles are Ta-rich and matrix is Ti-rich. The Zr presence is come from jar and balls used. The jar and balls were of Yttria stabilized zirconia, which is beneficial for Ti-based foams because promotes biocompatibility [73,74]. For this reason, jar and balls of Yttria stabilized zirconia were used. The sample with 9Sn show a microstructure composed of bimodal grain sizes, the larger grains are around of 20–40 μm (this grain size are no shown in Fig. 4c because the image has a magnification of 2000X). There is a chemical segregation of all elements, the grain boundaries are Ta-rich and grain centers are Ti-rich, Fig. 6a. The sample with 12Sn shows a microstructure with equiaxial grains with sizes smaller than 20 μm. Also, it is observed a chemical segregation of all elements, the grain boundaries are Ti-rich and grain centers are Ta-rich, Fig. 6b.

(b) Quantification of phases

Foam samples exhibit four phases, α-phase, β-phase, γ-phase, and YSZ particles (from jars and balls). The quantification of phases was done via the Rietveld method using MAUD software [76]. The microstructural model used for refinements was based on; the profile fittings that were performed by considering pseudo-Voight function, isotropic size–strain model, Delf line broadening model, without planar defects and arbitrary texture. Fig. 7 shows an example of Rietveld refinement for a foam with a composition Ti–13Ta–3Sn (All X-ray patters are given in supplementary materials). The quality of refinements is given by goodness of fit (GofF) and Rwp merit figure. A refinement is considered good when 1<GofF<2 and Rwp<10%. The results of the refinements showed that the GofF and Rwp values are smaller than 2 and

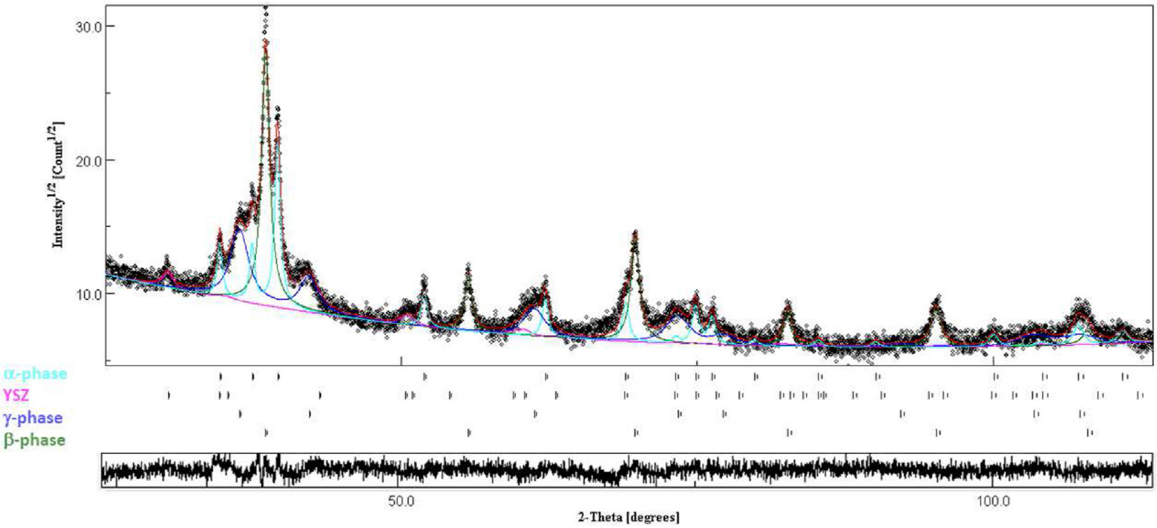

Fig. 7 – Rietveld refinement of X-ray diffraction pattern of foam of Ti–13Ta–3Sn alloy.

Table 1 – Quantification of phases present in the foams.

Composition foam, Ti–13Ta-xSn (at.%)	Milling time, h	α-phase, wt.%	β-phase, wt.%	γ-phase, wt.%	YSZ, %	Rwp, %	GofF
3Sn	30	34	55	8	3	10	1.0
6Sn	10	33	57	1	9	11	1.1
9Sn	10	41	58	0	1	11	1.1
12Sn	15	43	52	0	5	11	1.1

11%, respectively for all refinements, Table 1. The quantity of phases as a function of Sn amount is given in Table 1. It is possible to observe that all foams are composed mostly by mixing of α–phase and β-phase, over 89 wt.%. The quantity of α–phase increases with amount of Sn from 33 to 43 wt.%, the β-phase is relatively constant with a range between 52 and 58 wt.%, and the γ-phase is present only for foams with 3 and 6%Sn. In all samples, the presence of YSZ was observed and the foam with 6%Sn shows a higher amount of YSZ. No trend was observed between milling time, amount of Sn with the presence of YSZ. On the other hand, the amount of Sn and the milling times have a strong influence on the presence of three Ti-based phases. The α-Ti and β-Ti phases are equilibrium phases whereas γ-Ti is a metastable phase with a face centered-cubic, as it has been reported in some Ti-based alloys [45–47]. This phase is formed when to two conditions are achieved, high deformation and nanocrystalline grains size. In this case, both conditions are achieved during milling process.

(c) Characterization of porosity

Fig. 8 shows optical images of the foam pore distributions. For all specimens, relative homogeneous pore distribution is observed which is attributed to the powder mixing process, as well as acceptable segregation occurring during die filling. The features of pore distributions that are typical of metallic foams synthesized by the space holder method are (i) irregular thickness of cell edges produced by the agglomeration and shape of the space-holder particle, (ii) coalesced pores larger than NaCl particles size due to agglomeration of them, and (iii) the presence of regions that have a low quantity of pores [89]. Three types of pores were produced, (a) pores produced by NaCl particle dissolution with sizes ranging between 200 and 400 μm, (b) larger pores formed due to an agglomeration of NaCl particles, >400 μm and (c) smaller pores produced during the sintering process (equiaxialpores). The number of sintering pores is very high compared with the number of pores produced by the space-holder (by dissolution or coalescence). The porse shapes are cube-liked which are produced by the removal of NaCl. There are some pores with a flattened shape due to the consolidation process, where NaCl particles are deformed and fractured [90]. The shape of the largest pores is close to that of the ratio presented in human bones [52], benefitting the mechanical properties and osseointegration process [53].

The macro pore size distributions produced by the space-holder for all of the foams are given in Fig. 9, where it is possible to observe that they exhibit pore sizes that range from 100 to 500 μm. Fig. 9 shows the influence that Sn has on

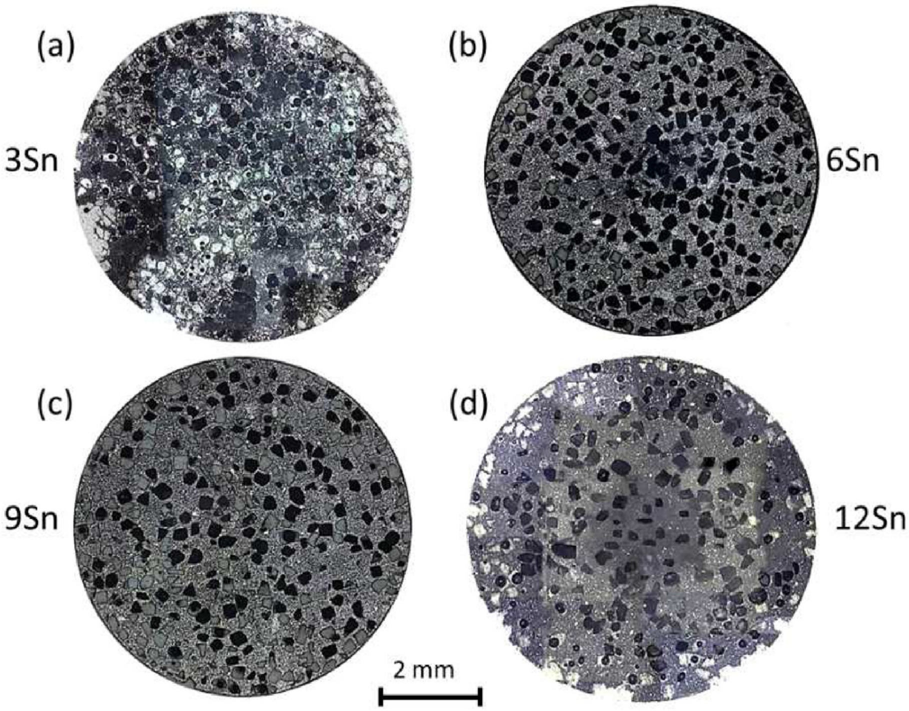

Fig. 8 – Optical images of foams, (a) Ti–13Ta–3Sn, (b) Ti–13Ta–6Sn, (c) Ti–13Ta–9Sn and (d) Ti–13Ta–12Sn.

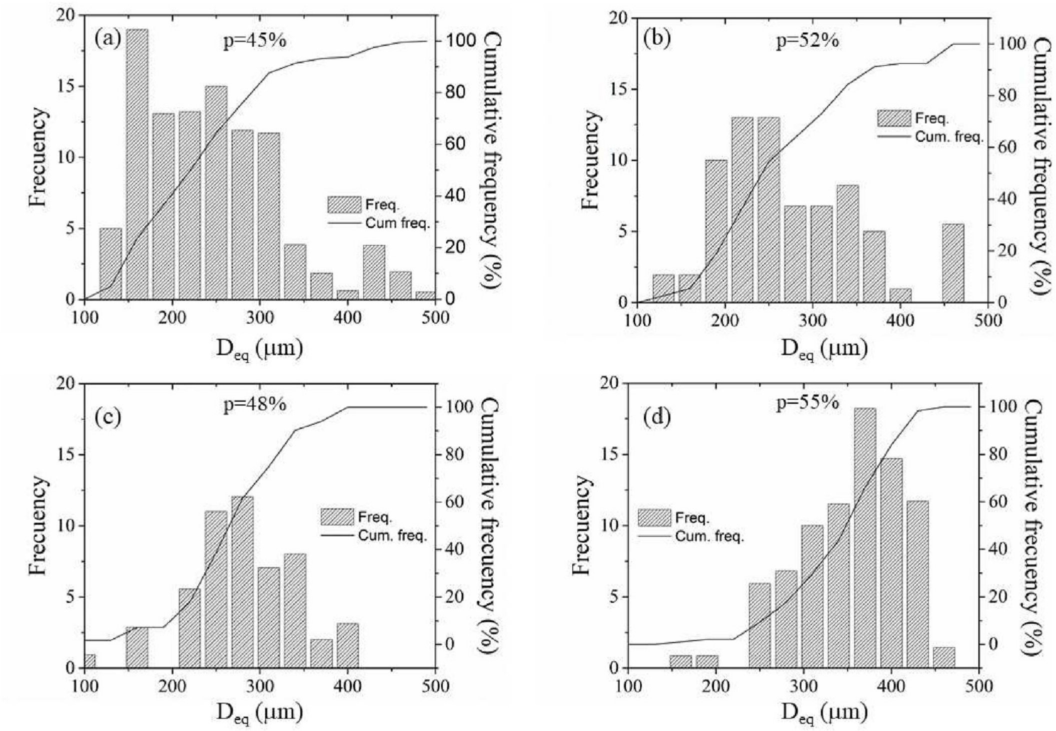

Fig. 9 – Macro pore size distribution for all samples, (a) Ti–13Ta–3Sn, (b) Ti–13Ta–6Sn, (c) Ti–13Ta–9Sn and (d) Ti–13Ta–12Sn.

macro pore size distribution, as Sn amount increases the macro pore size distribution is shifted to a higher pore size. For an amount of 3%Sn, the macro pore size range is around ~100–~350 μm and for an amount of 12%Sn, it is around ~250–~500 μm. The total porosities values measured by image analysis, p (%), are semi-closer to the nominal porosity value (50%). There is no clear trend in the amount of Sn versus the total porosity, because both Ti–13Ta–3Sn and Ti–13Ta–9Sn samples exhibited lower porosity than that of the nominal porosity value (50%), while the Ti–13Ta–6Sn and Ti–13Ta–12Sn samples showed higher total porosity than 50%. The macro pore size range is suitable to promote the growth of new bone tissue along with vascularization and osteointegration [11,91]. Similar results have been reported, e. i. Wen et al. [91] synthesized TiZr foams by using the space holder method with macro pore sizes of 200–500 μm, Nouri et al. [92] have reported a macro pore size of 350 μm for metallic foams of Ti–16Sn–4Nb alloys. Jha et al. [93] obtained pores smaller than 600 μm in pure Ti using a NaCl space-holder. Xiang et al. [94] obtained the distribution of pores between 200 and 500 μm in Ti foams using a $(NH_4)HCO_3$ space holder.

The micro pore size distributions produced by sintering are given in Fig. 10, where it is possible to observe that the highest D_{eq} values were around 100 μm. The fractions of the micro pore with sizes between 50 and 100 μm were lower compared with fractions of a smaller pore size (<50 μm). The average D_{eq} for all Ti–Ta-xSn alloys was between 14 and 21 μm. D_p is the density of the micro pore or pore quantity measured by unit of area, the smaller D_p value was 414 pore/μm for the Ti–13Ta–9Sn sample, with the highest value being 1759 pore/μm in the Ti–13Ta–12Sn sample. R pertains to the roundness (convexity), all samples exhibited R values close to 0.9. For R values between 0.7 and 1.0 the pore morphology is considered as semi or equiaxial. An R of 0.9 is in agreement with the semi-equiaxial morphology showed by pores originating from the sintering process. The sintering pores tend to be equiaxial, always minimizing surface energy [95], and pores produced by a NaCl particle dissolution showed cubic morphology. During the compaction process, they were fractured, deformed and re-arranged. Ff is the shape factor which was determined using the expression $F_f = 4\pi A/(PE)^2$ (A is the pore area and PE is the experimental perimeter of the pore). The F_f (isoperimetric quotient) is 1 for a circular shape. The F_f values were 0.84, 0.68, 0.66 and 0.87 for the samples with a Sn amount of 3, 6, 9, and 12%, respectively. These F_f values can be interpreted as the pore morphology being semi-equiaxial.

(d) Characterization of physical and mechanic properties

Fig. 11a presents the evolution of porosity and density. The density decreases as a function of the amount of Sn. Despite some foam samples showing a substantial error bar, there is a decrease of density from 2.85 to 2.67 g/cc. Note that the powders of different alloys were subjected to different milling times, so that a quantity of β-phase around of 55% could be achieved. Different phase ratios between α, β and γ-phase was obtained, which possibly influences the density, with them also showing to have different crystal structures. When the density decreases, the consolidating process was less efficient

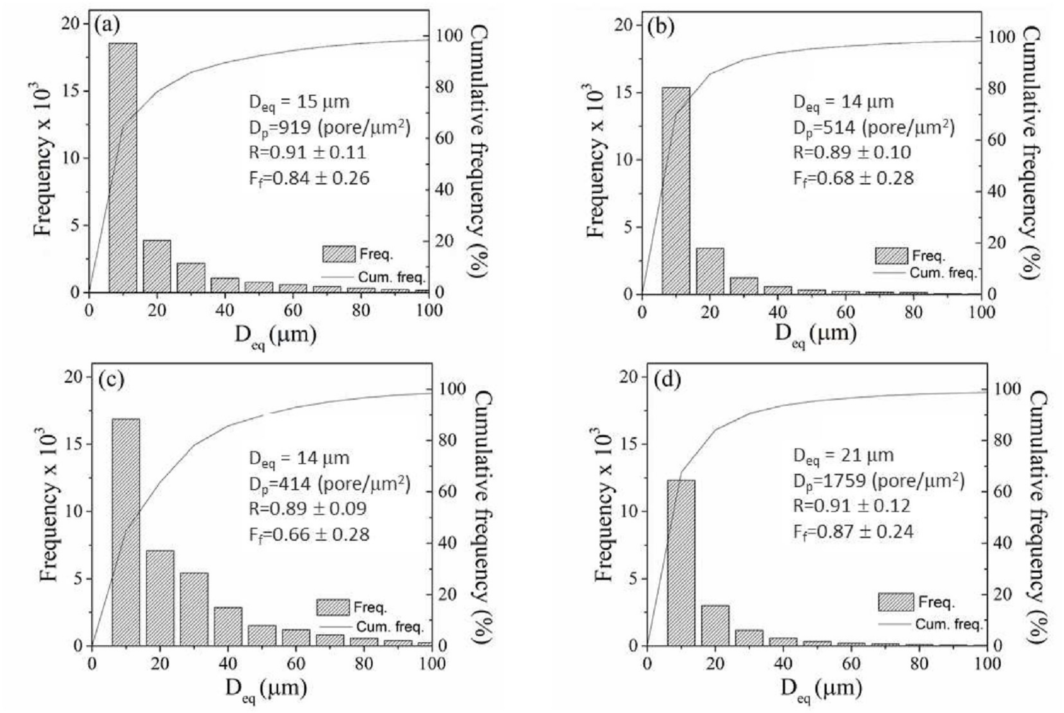

Fig. 10 – Micro pore size distribution for all samples, (a) Ti–13Ta–3Sn, (b) Ti–13Ta–6Sn, (c) Ti–13Ta–9Sn and (d) Ti–13Ta–12Sn.

[96]. On the other hand, the porosity increases with the amount of Sn. They increased from 53 to 59% for the amount of 3 and 12%Sn, respectively, indicating that all porosity values are over 50% of design porosity. The porosity is the relation between open pores and the external volume of a sample, without taking into account the closed pore [97]. The sintering process produce additional pores, therefore the porosity is the summation of porosity for the elimination of the space-holder and sintering pores. Another factor that can influence the density and porosity is the strength of the powders during the compaction process. When powders are harder, they exhibit a lower compaction capacity. During the compaction of metallic powders, two processes influence the green density, first the re-arrangement of particles, and second, the plastic deformation of particles [98]. The porosities measured by the Archimedes' method are higher than porosity values measured by image analysis, Fig. 6.

During the sintering process, several diffusion mechanisms are activated (surface, bulk, grain boundary) [99] producing a diminution of pore and consequently a shrinkage of samples due to atomic rearrangement. This shrinkage effect can be determined using Eq. (1) [100], where V is the original sample volume, h and r correspond to the height and radius of the cylindrical sample. The shrinkage decreases from ~-11 to ~ -2% for samples with Sn of 3 and 12%, respectively, Fig. 11b. Aguilar et al. [25] reported for Ti–34Nb–29Ta-xMn (x:2, 4 and 6 at%) foams shrinkage values of –14, –25 and –17%, respectively and Goi et al. [100] reported for Ti–Zr–Si foams shrinkage values between –1.4 and –50.1% depending on the experimental conditions of the consolidation process.

$$\frac{\Delta V}{V} \approx \frac{\Delta h}{h} + \frac{2\Delta r}{r} \tag{1}$$

Fig. 12a show the relationship between the Vickers microhardness with the Sn content in all of the foams. The microhardness values decrease from 530 to 450 HV (5,1 to 5,2 MPa) when the amount of Sn increases from 3 to 12%Sn, respectively. The microhardness values are influenced by several factors such as; (i) the microstructure, (ii) the amount of Sn in the alloys, (iii) the α/β phase ratio, (iv) microstrain, (v) crystallite size, and (vi) the amount of contamination coming from balls and jars. The higher microhardness values are obtained for 3 and 6Sn, which is coherent with the presence of dispersion of small second phase particles, Fig. 4a and b. The microhardness values for 9 and 12Sn are lower and show a large dispersion which is related with their microstructure type (mix of large and small grain sizes). In general, high hardness values were obtained in all foams, which is favorable since it has a high resistance to wear against the constant friction with the adjacent bone. Nouri et al. [92] reported a Vickers hardness between ~350 and ~580 (3432 to 5688 MPa) for Ti–16Sn–4Nb alloys obtained by ball-milled method. Sauceda et al. [101] measured a microhardness of around 450 HV (4410 MPa) in pure Ti foams. Jha et al. [93] synthetized Ti-foam using NaCl as the space holder and measured Vickers microhardness values between 258 and 263 kgf/mm^2 (2530 to

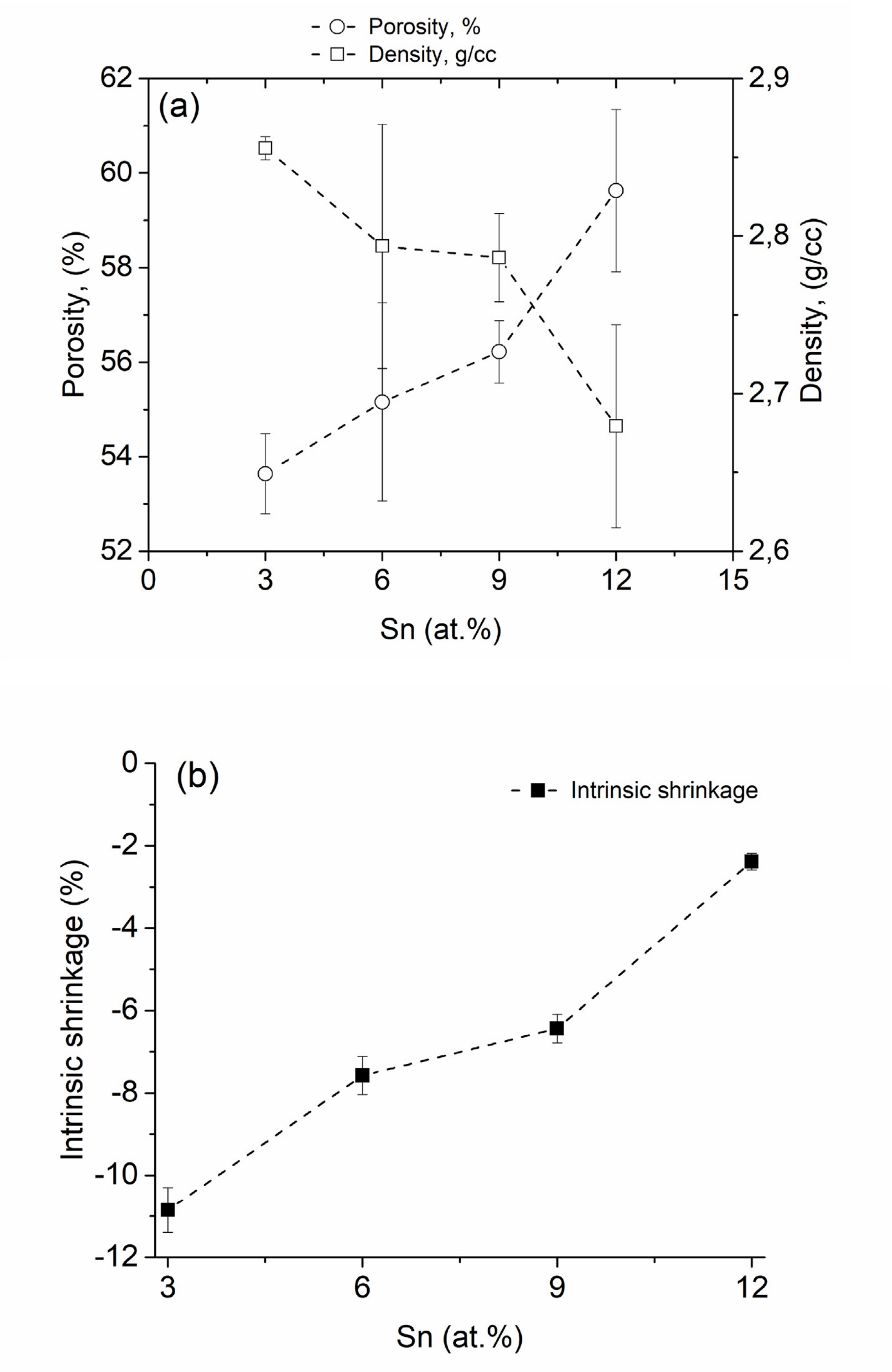

Fig. 11 – (a) Variation of porosity and density and (b) variation of intrinsic shrinkage as a function of Sn amount.

2579 MPa). Salvo et al. [102] measured a Vicker microhardness around 1 GPa for Ti–30Nb–13Ta–2Mn (wt. %) foams. Abhash el al [103]. measured the Vickers microhardness values of Ti–6Al-xCo (x:2, 5 and 8 wt.%) foams with average values being 509, 648 and 793 kgf/mm^2 (4,991, 6354 and 7776 MPa) for 2, 5 and 8 of Co, respectively.

A similar trend of change in the yield strength values as a function to the amount of Sn was observed. The values decreased from 176 to 151 MPa for 3 and 12%Sn, respectively, Fig. 12b. Compressive yield strength of metallic foams over 120 MPa are acceptable to be used as biomaterials [104]. Salvo et al. [105] studied the compressive strength of Ti–30Nb–13Ta–2Mn (wt. %) foams (consolidated by hot-pressing process) and reported yield strength values between 180 and 400 MPa for a level porosity of 30%. Sauceda et al. [101] reported a compressive yield strength of 24 and 16 MPa for Ti

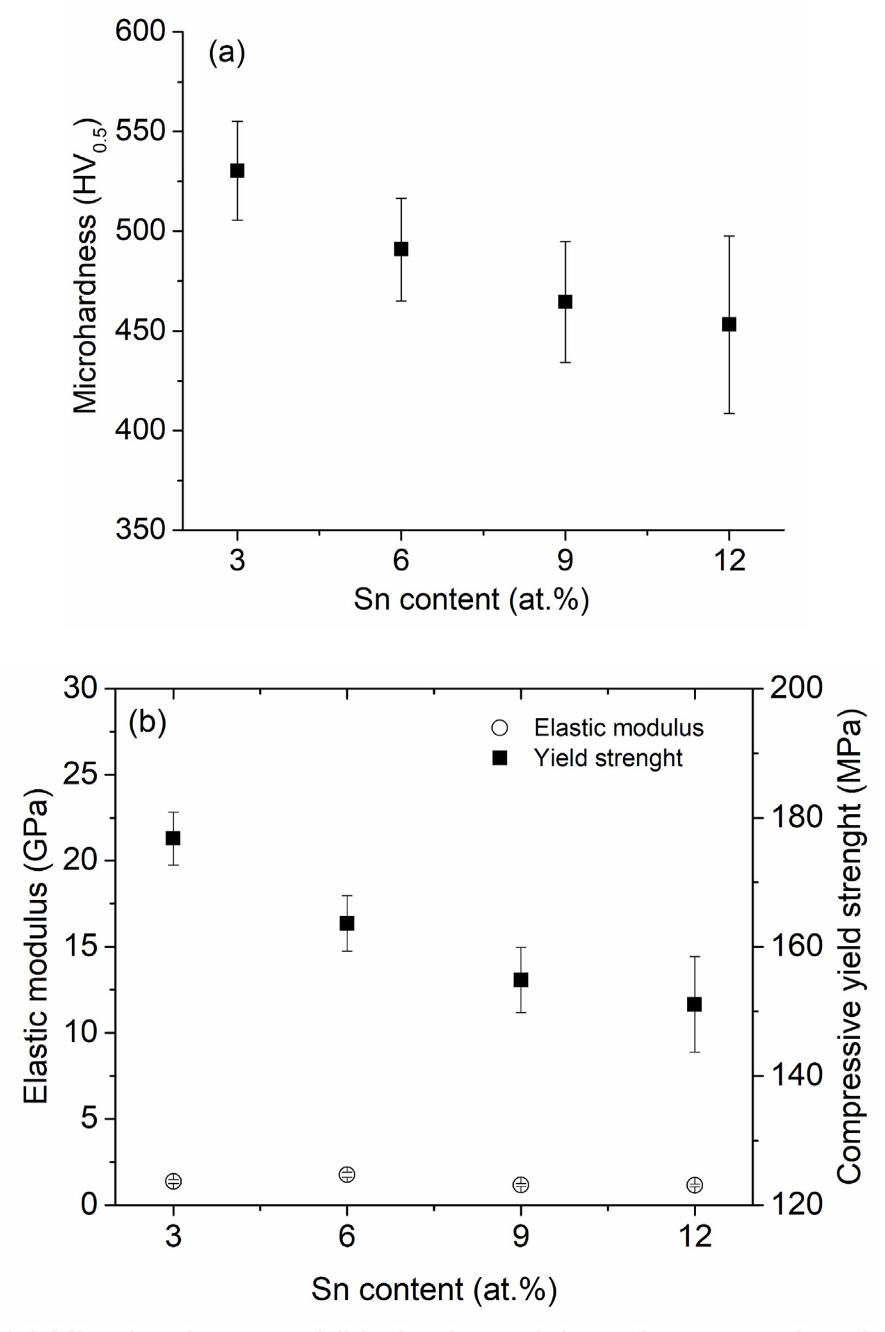

Fig. 12 – (a) Microhardness and (b) elastic module and compressive yield strength of foams with different amounts of Sn (Ti–13Ta–xSn, x:3, 6, 9 and 12 at.%).

foams with 50% porosity synthesized by simple action die and floating action die, respectively. Aguilar et al. [25] measured compressive yield strengths between 22 and 55 MPa for Ti–34Nb–29Ta–xMn (x: 2, 4 and 6 wt.%Mn) alloy foams with 50% porosity (consolidated by traditional sintering process). The density is the most important variable that influences the properties of metallic foams such as, strength and elastic modulus [106]. There was a relationship between density and yield strength, both decreasing. In metallic foams, there were micro flaws in pore walls, which promotes the diminution of strength. In the compressive test, macroscopic crack propagation resulted in an abrupt load drop. The strength of metallic foams was strongly influenced by the thicker pore walls and smaller pore diameters, and less influenced by the morphology of pore walls, with pore sizes having little effect on the strength of a metallic foam [107]. When powders used to synthesized foams were obtained through milling, the work-hardening affects the particle packing characteristics modifying its densification in sintering stage of powder metallurgy [95]. The elastic modulus values changed slightly with the amount of Sn from

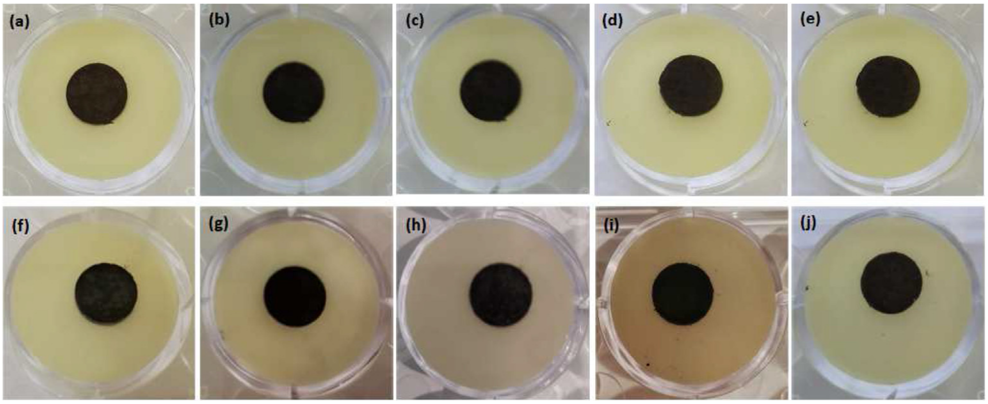

Fig. 13 – Digital images of Ti–13Ta–xSn after exposure to liquid agar medium inoculated with (a–e) *Staphylococcus aureus* and (f–j) *Escherichia coli*. (a,f) x = 0, (b,g) x = 3, (c,h) x = 6, (d,i) x = 9, and (e,j) x = 12.

~2 to ~1 GPa, Fig. 12b. The elastic modulus values obtained were within the range of trabecular bone which has an elastic modulus between 0.4 and 4 GPa [33]. In the literature there exists a wide range of elastic modulus values reported for Ti foams and Ti-based alloys foams. Guerra et al. [21] reported elastic modulus between 4,5; 8,8; and 11.7 GPa (37, 31, and 25% of porosity) for Ti–20Nb–11Ta–16Fe–1Mn at.% alloys foams. Aguilar et al. [25] reported that for a foam with a porosity of 50v/v% in Ti–34Nb–29Ta-xMn (x:2, 4 and 6 wt.%Mn) alloys, the Young's modulus values were between 25 and 33 GPa. Singh et al. [108] measured Young's modulus values between 5 and 24 GPa for Ti4wt%Al foam with porosities of 85 and 50%l, respectively. Martinez et al. [109] measured Young's modulus values of 110, 5.6, and 3.2 GPa for porosities of 0, 21, and 42%, respectively in a traditional Ti–6Al–4V alloy. Said alloy also showed Young's modulus values between 2.0 and 2.6 GPa when having a level porosity of 81.5 and 80.1%, as reported by Chen et al. [110]. Ye and Dunand [90] synthesized pure Ti foams by hot pressing and reported a Young's modulus between 39 and 29 GPa for porosities between 52 and 51%.

3.3. *Characterization of antibacterial properties*

Ti-based alloys are widely used in the medical industry due to them providing better adhesion and contact between implant and surrounding tissues when compared to other materials. However, one of the disadvantages that impede their wider clinical use is the potential septic and aseptic failure, as was mentioned above. In particular, some studies related to bacterial adhesion and biofilm formation on porous Ti-based alloys have been performed. For instance, Domínguez et al. [61] suggested a lower colonization of *E. coli* and *Pseudomonas aeruginosa* for bulk in comparison to the porous cp-Ti. The authors proposed that the bacterial growth was influenced by the morphology of the samples. Furthermore, Civantos et al. [62] observed that when a porous CP-Ti was exposed to *E. coli*, the pore size showed a higher contribution than the roughness. Recently, Silva et al. [68] found that the presence of *S. aureus* in a simulated biofluid solution influenced the composition of the oxide layer of Ti–6Al–4V, which was more drastic when porosity was added. In this work, a microbial growth analysis using a gram-positive bacterium, *S. aureus*, and a gram-negative bacterium, *E. coli*, was performed. These test strains were considered due to both bacteria being able to adhere to several types of surfaces [111], which can influence the corrosion resistance of metals. *E. coli* is frequently found in the human gut, hands and feet [112], while *S. aureus* is typically transmitted during hospital stays. Indeed, *S. aureus* [64] and *S. epidermidis* [64,113] are bacteria frequently associated to infections associated with implants, which may produce inflammation, pain, allergic reaction, and infection [64,113].

In this work, negative, positive, and neutral controls were also used for analyzing the antibacterial properties of Ti-13-xSn alloys after exposure to agar medium inoculated with *S. aureus* and *E. coli* (not shown here). Keeping the optical density close to 0.1, digital images of Ti-13-xSn alloy samples were taken after an 18 h exposure to an agar medium sterilized and inoculated with both bacteria, Fig. 13. It should be noted that no antibacterial activity was revealed by the samples under these conditions. Also, bacterial adhesion or biofilm formation related to the presence of *S. aureus* or *E. coli* on foam surfaces was not observed under the conditions tested. This could suggest inhibition of these usual bacterial processes. Bacterial adhesion inhibition on a bio-implant surface is indispensable to minimize the possibility of infections. However, future studies should test longer periods of incubation. Bacterial adhesion inhibition on a bio-implant surface is indispensable to minimize the possibility of infections. This has previously been attributed to the passive/oxide film dissolution and the Ti-alloy passive nature, as was described by Naiming et al. [114]. However, the surface roughness and irregularities can influence the antibacterial activity due to the increase in surface density decreasing the surface contact area through the bacterial membrane, being mainly diminished for gram-positive bacteria adhesion on the surface, as reported by Whitehead et al. [115] and Bagherifard et al. [116].

4. Conclusions

In this work, the influence that the amount of Sn has on the mechanical properties and the antibacterial response of α/β-ternary Ti-based alloy (Ti–13Ta–xSn, x:3, 6, 9, and 12 at.%) has been studied.

The Ti-based alloy foams were composed mostly by a mix of both α–phase and β-phase (over 89 wt.%) plus an amount of γ–phase and YSZ particles from jars and balls. The foams mainly exhibited the presence of the β-phase which is preferable in reducing the elastic modulus. The presence of γ–phase was observed only for metallic foams with amounts of 3 and 6% Sn. The metallic foams exhibited relative homogeneous pore distribution with sizes between 100 and 450 μm and an average porosity slightly higher than 50%. Also, the samples exhibited interconnected porosity. All features mentioned are suitable to promote cell adhesion and bone growth.

Concerning the mechanical properties, the foams showed elastic modulus values between 1 and 2 GPa, compressive yield strengths over 150 MPa, and a microhardness over 450 HV. In addition, they showed no antibacterial activity *E. coli* and *S. aureus* microorganisms under the conditions tested, but neither was bacterial adhesion observed indicating that there is a bacterial adhesion inhibition. This is important because of the potential to reduce the possibility of infections.

In summary, considering following aspects, (i) relatively homogeneous pore distribution with sizes similar to those of human bone, (ii) mechanical properties meet the requirements of human bone and (ii) no antibacterial activity and neither bacterial adhesion was observed, the Ti-based alloy foams have the potential to be explored for biomedical applications, especially those related to trabecular bones.

Author contributions

C. Aguilar: Conceptualization, Formal analysis, Funding acquisition, Investigation, Methodology, Project administration, Resources, Supervision, Writing - original draft, Writing - review & editing.

F. San Martín: Formal analysis, Visualization, Writing - original draft.

C. Martínez: Formal analysis, Investigation, Project administration, Supervision, Visualization, Writing - original draft, Writing - review & editing.

B. Cámara: Formal analysis, Investigation, Methodology, Supervision, Writing - review & editing.

F. Claverías: Data curation, Formal analysis, Methodology.

A. Undabarrena: Data curation, Formal analysis, Methodology.

M. Sancy: Formal analysis, Visualization, Writing - original draft.

V. Salinas: Data curation, Methodology.

L. Muñoz: Conceptualization, Data curation, Investigation, Methodology.

Declaration of Competing Interest

The authors declare that they have no known competing financial interests or personal relationships that could have appeared to influence the work reported in this paper.

Acknowledgments

This work was funded by the Millennium Institute on Green Ammonia as Energy Vector - MIGA (ICN2021_023) supported by the Millennium Scientific Initiative, and by FONDECYT n°1190797, FONDECYT n° 1230620, FONDEQUIP n° EQM140095 FONDECYT Initiation n°11220774 of the Agencia Nacional de Investigación y Desarrollo (ANID).

REFERENCES

[1] Li P, Ma X, Tong T, Wang Y. Microstructural and mechanical properties of β-type Ti–Mo–Nb biomedical alloys with low elastic modulus. J Alloys Compd 2020;815:152412. https://doi.org/10.1016/j.jallcom.2019.152412.

[2] Rajabi F, Zarei Hanzaki A, Abedi HR, Farghadany E. Corrosion behavior of thermo-mechanically processed biomedical Ti-29Nb-13Ta-4.6Zr. J Alloys Compd 2017;725:23–31. https://doi.org/10.1016/j.jallcom.2017.04.319.

[3] Yan S, Song GL, Li Z, Wang H, Zheng D, Cao F, et al. A state-of-the-art review on passivation and biofouling of Ti and its alloys in marine environments. J Mater Sci Technol 2018;34:421–35. https://doi.org/10.1016/j.jmst.2017.11.021.

[4] Biesiekierski A, Wang J, Gepreel MA, Wen C. A new look at biomedical Ti-based shape memory alloys. Acta Biomater 2012;8:1661–9. https://doi.org/10.1016/j.actbio.2012.01.018.

[5] Singh P, Pungotra H, Kalsi NS. On the characteristics of titanium alloys for the aircraft applications. Mater Today Proc 2017;4:8971–82. https://doi.org/10.1016/j.matpr.2017.07.249.

[6] Ishida T, Wakai E, Hagiwara M, Makimura S, Tada M, Asner DM, et al. Study of the radiation damage effect on Titanium metastable beta alloy by high intensity proton beam. Nucl Mater Energy 2018;15:169–74. https://doi.org/10.1016/j.nme.2018.04.006.

[7] Ivlev I, Vacek J, Kneppo P. Multi-criteria decision analysis for supporting the selection of medical devices under uncertainty. Eur J Oper Res 2015;247:216–28. https://doi.org/10.1016/j.ejor.2015.05.075.

[8] Pruchova E, Kosova M, Fojt J, Jarolimova P, Jablonska E, Hybasek V, et al. A two-phase gradual silver release mechanism from a nanostructured TiAlV surface as a possible antibacterial modification in implants. Bioelectrochemistry 2019;127:26–34. https://doi.org/10.1016/j.bioelechem.2019.01.003.

[9] Karacan I, Ben-Nissan B, Wang HA, Juritza A, Swain MV, Müller WH, et al. Mechanical testing of antimicrobial biocomposite coating on metallic medical implants as drug delivery system. Mater Sci Eng, C 2019;104. https://doi.org/10.1016/j.msec.2019.109757.

[10] Ferraris S, Spriano S. Antibacterial titanium surfaces for medical implants. Mater Sci Eng, C 2016;61:965–78. https://doi.org/10.1016/j.msec.2015.12.062.

[11] Geetha M, Singh AK, Asokamani R, Gogia AK. Ti based biomaterials , the ultimate choice for orthopaedic implants – a review. Prog Mater Sci 2009;54:397–425. https://doi.org/10.1016/j.pmatsci.2008.06.004.

[12] Elias CN, Lima JHC, Valiev R, Meyers MA. Biomedical applications of titanium and its alloys. Biol Mater Sci 2008:1–4.

[13] Niinomi M. Mechanical biocompatibilities of titanium alloys for biomedical applications. J Mech Behav Biomed Mater 2008;1:30–42. https://doi.org/10.1016/j.jmbbm.2007.07.001.

[14] Abdel-Hady Gepreel M, Niinomi M. Biocompatibility of Ti-alloys for long-term implantation. J Mech Behav Biomed Mater 2013;20:407–15. https://doi.org/10.1016/j.jmbbm.2012.11.014.

[15] Kawahara M, Kato-Negishi M. Link between aluminum and the pathogenesis of Alzheimer's disease: the integration of the aluminum and amyloid cascade hypotheses. Int J Alzheimer's Dis 2011;2011. https://doi.org/10.4061/2011/276393.

[16] Okazaki Y. A new Ti-15Zr-4Nb-4Ta alloy for medical applications. Curr Opin Solid State Mater Sci 2001;5:45–53. https://doi.org/10.1016/S1359-0286(00)00025-5.

[17] Thompson GJ, Puleo DA. Ti-6Al-4V ion solution inhibition of osteogenic cell phenotype as a function of differentiation timecourse in vitro. Biomaterials 1996:1949–54.

[18] Nag S, Banerjee R, Fraser HL. Microstructural evolution and strengthening mechanisms in Ti-Nb-Zr-Ta, Ti-Mo-Zr-Fe and Ti-15Mo biocompatible alloys. Mater Sci Eng, C 2005;25:357–62. https://doi.org/10.1016/j.msec.2004.12.013.

[19] Jaishankar M, Tseten T, Anbalagan N, M BB, Beeregowda KN. Toxicity, mechanism and health effects of some heavy metals. Toxicology 2014:60–72.

[20] Yang MH, Chen SC, Lin YF, Lee YC, Huang MY, Chen KC, et al. Reduction of aluminum ion neurotoxicity through a small peptide application – NAP treatment of Alzheimer's disease. J Food Drug Anal 2019;27:551–64. https://doi.org/10.1016/j.jfda.2018.11.009.

[21] Guerra C, Sancy M, Walczak M, Martínez C, Ringuedé A, Cassir M, et al. Effect of added porosity on a novel porous Ti-Nb-Ta-Fe-Mn alloy exposed to simulated body fluid. Mater Sci Eng, C 2020;111. https://doi.org/10.1016/j.msec.2020.110758.

[22] Huiskes R, Weinans H, Van Rietbergen B. The relationship between stress shielding and bone resorption around total hip stems and the effects of flexible materials. Clin Orthop Relat Res 1992:124–34. https://doi.org/10.1097/00003086-199201000-00014.

[23] Luo JP, Huang YJ, Xu JY, Sun JF, Dargusch MS, Hou CH, et al. Additively manufactured biomedical Ti-Nb-Ta-Zr lattices with tunable Young's modulus: mechanical property, biocompatibility, and proteomics analysis. Mater Sci Eng, C 2020;114. https://doi.org/10.1016/j.msec.2020.110903.

[24] Liu J, Yang Q, Yin J, Yang H. Effects of alloying elements and annealing treatment on the microstructure and mechanical properties of Nb-Ta-Ti alloys fabricated by partial diffusion for biomedical applications. Mater Sci Eng, C 2020;110:110542. https://doi.org/10.1016/j.msec.2019.110542.

[25] Aguilar C, Guerra C, Lascano S, Guzman D, Rojas PA, Thirumurugan M, et al. Synthesis and characterization of Ti-Ta-Nb-Mn foams. Mater Sci Eng, C 2016;58. https://doi.org/10.1016/j.msec.2015.08.053.

[26] Mohammed MT, Khan ZA, Geetha M. Effect of thermo-mechanical processing on microstructure and electrochemical behavior of Ti-Nb-Zr-V new metastable β titanium biomedical alloy. Trans Nonferrous Met Soc China (English Ed 2015;25:759–69. https://doi.org/10.1016/S1003-6326(15)63661-5.

[27] Fellah M, Hezil N, Abdul Samad M, Djellabi R, Montagne A, Mejias A, et al. Effect of molybdenum content on structural, mechanical, and tribological properties of hot isostatically pressed β-type titanium alloys for orthopedic applications. J Mater Eng Perform 2019;28:5988–99. https://doi.org/10.1007/s11665-019-04348-w.

[28] Liu H, Yang J, Zhao X, Sheng Y, Li W, Chang CL, et al. Microstructure, mechanical properties and corrosion behaviors of biomedical Ti-Zr-Mo-xMn alloys for dental application. Corrosion Sci 2019;161:108195. https://doi.org/10.1016/j.corsci.2019.108195.

[29] Zhao X, Niinomi M, Nakai M, Ishimoto T, Nakano T. Development of high Zr-containing Ti-based alloys with low Young's modulus for use in removable implants. Mater Sci Eng, C 2011;31:1436–44. https://doi.org/10.1016/j.msec.2011.05.013.

[30] Tan MHC, Baghi AD, Ghomashchi R, Xiao W, Oskouei RH. Effect of niobium content on the microstructure and Young's modulus of Ti-xNb-7Zr alloys for medical implants. J Mech Behav Biomed Mater 2019;99:78–85. https://doi.org/10.1016/j.jmbbm.2019.07.014.

[31] Zhou YL, Niinomi M, Akahori T. Effects of Ta content on Young's modulus and tensile properties of binary Ti-Ta alloys for biomedical applications. Mater Sci Eng A 2004;371:283–90. https://doi.org/10.1016/j.msea.2003.12.011.

[32] Sanchez-molina D, Velazquez-ameijide J, Quintana V, Arregui-dalmases C, Crandall JR, Subit D, et al. Fractal dimension and mechanical properties of human cortical bone. Med Eng Phys 2013;35:576–82. https://doi.org/10.1016/j.medengphy.2012.06.024.

[33] Wu D, Isaksson P, Ferguson SJ, Persson C. Young ' s modulus of trabecular bone at the tissue level : a review. Acta Biomater 2018;78:1–12. https://doi.org/10.1016/j.actbio.2018.08.001.

[34] Cai X, Follet H, Peralta L, Gardegaront M, Farlay D, Gauthier R, et al. Anisotropic elastic properties of human femoral cortical bone and relationships with composition and microstructure in elderly. Acta Biomater 2019;90:254–66. https://doi.org/10.1016/j.actbio.2019.03.043.

[35] Liu Y, Jiang G, He G. Enhancement of entangled porous titanium by BisGMA for load-bearing biomedical applications. Mater Sci Eng, C 2016;61:37–41. https://doi.org/10.1016/j.msec.2015.12.018.

[36] Lee SW, Kim JH, Park CH, Hong JK, Yeom JT. Alloy design of metastable $\alpha+\beta$ titanium alloy with high elastic admissible strain. Mater Sci Eng A 2021;802:140621. https://doi.org/10.1016/j.msea.2020.140621.

[37] Zhou L, Chen J, Huang WY, Ren Y, Niu Y, Yuan T. Effects of Ta content on phase transformation in selective laser melting processed Ti-13Nb-13Zr alloy and its correlation with elastic properties. Vacuum 2021;183:109798. https://doi.org/10.1016/j.vacuum.2020.109798.

[38] Zhang J, Ke W, Ji W, Fan Z, Wang W, Fu Z. Microstructure and properties of insitu titanium boride (TiB)/titanium (TI) composites. Mater Sci Eng A 2015;648:158–63. https://doi.org/10.1016/j.msea.2015.09.067.

[39] Sun F, Huang L, Zhang R, Wang S, Jiang S, Sun Y, et al. In-situ synthesis and superhigh modulus of network structured TiC/Ti composites based on diamond-Ti system. J Alloys Compd 2020;834:1–11. https://doi.org/10.1016/j.jallcom.2020.155248.

[40] Aguilar C, Arancibia M, Alonso I, Sancy M, Tello K. Influence of porosity on the elastic modulus of Ti-Zr-Ta-Nb foams with a low Nb content. Metals (Basel) 2019;9:1–15. https://doi.org/10.3390/met9020176.

[41] Li Y, Xiong J, Wong CS, Hodgson PD, Wen C. Ti6Ta4Sn alloy and subsequent scaffolding for bone tissue engineering. Tissue Eng 2009;15:3151–9. https://doi.org/10.1089/ten.TEA.2009.0150.

[42] Singh R, Lee PD, Dashwood RJ, Lindley TC. Titanium foams for biomedical applications: a review. Mater Technol 2010;25:127–36. https://doi.org/10.1179/175355510X12744412709403.

[43] Arabnejad S, Johnston RB, Ann J, Singh B, Tanzer M, Pasini D. High-strength porous biomaterials for bone replacement : a strategy to assess the interplay between cell morphology , mechanical properties , bone ingrowth and manufacturing constraints. Acta Biomater 2016;30:345–56. https://doi.org/10.1016/j.actbio.2015.10.048.

[44] Niinomi M. Recent research and development in metallic materials for biomedical, dental and healthcare products applications. Mater Sci Forum 2007;539–543:193–200. https://doi.org/10.4028/www.scientific.net/msf.539-543.193.

[45] Aguilar C, Pio E, Medina A, Mangalaraja RV, Salvo C, Alfonso I, et al. Structural study of novel nanocrystalline fcc Ti-Ta-Sn alloy. Metall Mater Trans A Phys Metall Mater Sci 2019;50. https://doi.org/10.1007/s11661-019-05152-w.

[46] Prasanthi TN, Sudha C, Ravikirana, Saroja S. Formation and reversion of metastable fcc phase in a Ti-5Ta-2Nb explosive clad. Mater Char 2016;116:24–32. https://doi.org/10.1016/j.matchar.2016.03.022.

[47] Bolokang AS, Phasha MJ, Motaung DE, Cummings FR, Muller TFG, Arendse CJ. Microstructure and phase transformation on milled and unmilled Ti induced by water quenching. Mater Lett 2014;132:157–61. https://doi.org/10.1016/j.matlet.2014.06.063.

[48] Dercz G, Matu I, Zubko M, Kazek-k A, Maszybrocka J. Synthesis of porous Ti – 50Ta alloy by powder metallurgy. Mater Character 2018;142:124–36. https://doi.org/10.1016/j.matchar.2018.05.033.

[49] Chinnappan R, Panigrahi BK, van de Walle A. First-principles study of phase equilibrium in Ti–V, Ti–Nb, and Ti–Ta alloys. Calphad Comput Coupling Phase Diagrams Thermochem 2016;54:125–33. https://doi.org/10.1016/j.calphad.2016.07.001.

[50] A. International. ASM Handbook: alloy phase diagrams, vol. 3. Metals Park, OH: Alloy phase diagrams: ASM; 1992. 1992.

[51] Tan J, Xu G, Tao X, Chen F, Cui Y, Zhou L. CALPHAD assessment of bio-oriented Ti–Zr–Sn system and experimental validation in Ti/Zr-rich alloys. Calphad Comput Coupling Phase Diagrams Thermochem 2019;67:101686. https://doi.org/10.1016/j.calphad.2019.101686.

[52] Selvinsimpson S, Gnanamozhi P, Pandiyan V, Govindasamy M, Habila MA, AlMasoud N, et al. Synergetic effect of Sn doped ZnO nanoparticles synthesized via ultrasonication technique and its photocatalytic and antibacterial activity. Environ Res 2021;197:111115. https://doi.org/10.1016/j.envres.2021.111115.

[53] Schildhauer TA, Robie B, Muhr G, Köller M. Bacterial adherence to tantalum versus commonly used orthopedic metallic implant materials. J Orthop Trauma 2006;20:476–84.

[54] Vasanthi M, Ravichandran K, Jabena Begum N, Muruganantham G, Snega S, Panneerselvam A, et al. Influence of Sn doping level on antibacterial activity and certain physical properties of ZnO films deposited using a simplified spray pyrolysis technique. Superlattice Microst 2013;55:180–90. https://doi.org/10.1016/j.spmi.2012.12.011.

[55] Wang X, Ning B, Pei X. Tantalum and its derivatives in orthopedic and dental implants: osteogenesis and antibacterial properties. Colloids Surf B Biointerfaces 2021. https://doi.org/10.1016/j.colsurfb.2021.112055.

[56] Song Y, Xu DS, Yang R, Li D, Wu WT, Guo ZX. Theoretical study of the effects of alloying elements on the strength and modulus of beta -type bio-titanium alloys. Mater Sci Eng A 1999;260:269–74.

[57] Alves AC, Sendão I, Ariza E, Toptan F, Ponthiaux P, Pinto AMP, et al. Corrosion behaviour of porous Ti intended for biomedical applications. J Porous Mater 2016;23:1261–8. https://doi.org/10.1016/j.msec.2018.11.025.

[58] Li YH, Chen N, Cui HT, Wang F. Fabrication and characterization of porous Ti–10Cu alloy for biomedical application. J Alloys Compd 2017;723:967–73. https://doi.org/10.1016/j.jallcom.2017.06.321.

[59] Sri Maha Vishnu D, Sure J, Liu Y, Vasant Kumar R, Schwandt C. Electrochemical synthesis of porous Ti-Nb alloys for biomedical applications. Mater Sci Eng, C 2019;96:466–78. https://doi.org/10.1016/j.msec.2018.11.025.

[60] Xie FX, He XB, Cao SL, Lu X, Qu XH. Structural characterization and electrochemical behavior of a laser-sintered porous Ti-10Mo alloy. Corrosion Sci 2013;67:217–24. https://doi.org/10.1016/j.corsci.2012.10.036.

[61] Domínguez-Trujillo C, Beltrán AM, Garvi MD, Salazar-Moya A, Lebrato J, Hickey DJ, et al. Bacterial behavior on coated porous titanium substrates for biomedical applications. Surf Coating Technol 2019;357:896–902. https://doi.org/10.1016/j.surfcoat.2018.10.098.

[62] Civantos A, Beltrán AM, Domínguez-Trujillo C, Garvi MD, Lebrato J, Rodríguez-Ortiz JA, et al. Balancing porosity and mechanical properties of titanium samples to favor cellular growth against bacteria. Metals (Basel) 2019;9:1–16. https://doi.org/10.3390/met9101039.

[63] Zhang F, Zhang Z, Zhu X, Kang ET, Neoh KG. Silk-functionalized titanium surfaces for enhancing osteoblast functions and reducing bacterial adhesion. Biomaterials 2008;29:4751–9. https://doi.org/10.1016/j.biomaterials.2008.08.043.

[64] Sarker A, Tran N, Rifai A, Brandt M, Tran PA, Leary M, et al. Rational design of additively manufactured Ti6Al4V implants to control Staphylococcus aureus biofilm formation. Materialia 2019;5:100250. https://doi.org/10.1016/j.mtla.2019.100250.

[65] Oliveira WF, Silva PMS, Silva RCS, Silva GMM, Machado G, Coelho LCBB, et al. Staphylococcus aureus and Staphylococcus epidermidis infections on implants. J Hosp Infect 2018;98:111–7. https://doi.org/10.1016/j.jhin.2017.11.008.

[66] Ziąbka M, Kiszka J, Trenczek-Zając A, Radecka M, Cholewa-Kowalska K, Bissenik I, et al. Antibacterial composite hybrid coatings of veterinary medical implants. Mater Sci Eng, C 2020;112. https://doi.org/10.1016/j.msec.2020.110968.

[67] Gnanamani A, Hariharan P, Paul-Satyaseela M. Staphylococcus aureus: overview of bacteriology, clinical diseases, epidemiology, antibiotic resistance and therapeutic approach. Front Staphylococcus Aureus 2017:4–28. https://doi.org/10.5772/67338.

[68] Silva D, Guerra C, Muñoz H, Aguilar C, Walter M, Azocar M, et al. The effect of Staphylococcus aureus on the electrochemical behavior of porous Ti-6Al-4V alloy. Bioelectrochemistry 2020;136. https://doi.org/10.1016/j.bioelechem.2020.107622.

[69] Erjavec MS. Introductory chapter: the versatile Escherichia coli. In: Universe *Escherichia coli*. IntechOpen; 2019.

[70] Sakaguchi N, Niinomi M, Akahori T, Takeda J, Toda H. Effect of Ta content on mechanical properties of Ti-30Nb-XTa-5Zr. Mater Sci Eng, C 2005;25:370–6. https://doi.org/10.1016/j.msec.2005.04.003.

[71] M. Peters, Titanium and titanium alloys Edited by, [n.d].

[72] Aguilar C, Martin P, Pio E, Salvo C, Neves GO. Materials analysis applying thermodynamic (MAAT) software: a friendly and free tool to analyze the formation of solid solutions, amorphous phases and intermetallic compounds. Comput Phys Commun 2021;259. https://doi.org/10.1016/j.cpc.2020.107573.

[73] Saravanan G, Bavanilathamuthiah M, Kirubaharan K, Ramachandran D, Dharini T, Viswanathan K, et al. Bio-inspired YSZ coated titanium by EB-PVD for biomedical applications. Surf Coat Technol 2016;307:227–35. https://doi.org/10.1016/j.surfcoat.2016.08.039.

[74] Dantas TA, Pinto P, Vaz PCS, Silva FS, Cam CAD. Design and optimization of zirconia functional surfaces for dental implants applications. Ceram Int 2020;46:16328–36. https://doi.org/10.1016/j.ceramint.2020.03.190.

[75] Aguilar C, Pio E, Medina A, Martínez C, Sancy M, Guzman D. Evolution of synthesis of FCC nanocrystalline solid solution and amorphous phase in the Ti-Ta based alloy by high milling energy. J Alloys Compd 2020:155980. https://doi.org/10.1016/j.jallcom.2020.155980.

[76] Lutterotti L, Matthies S, Wenk HR. MAUD: a friendly Java program for material analysis using diffraction. Newsl CDP 1999;21:14–5.

[77] Lutterotti L, Scardi P. Simultaneous structure and size–strain refinement by the Rietveld method. J Appl Crystallogr 1990;23:246–52. https://doi.org/10.1107/S0021889890002382.

[78] Scardi P, Lutterotti L, Maistrelli P. Experimental determination of the instrumental broadening in the Bragg–Brentano geometry. Powder Diffr 1994;9:180–6. https://doi.org/10.1017/S0885715600019187.

[79] Delhez EJ, de Keijser R, Th H, Langford JI, Louër D, Mittemeijer EJ, et al. Crystal imperfection broadening and peak shape in the Rietveld method" in "The Rietveld Method. Oxford, UK: Oxford Uni; 1993.

[80] de Keijser TH, Langford JI, Mittemeijer EJ, Vogels ABP. Use of the Voigt function in a single-line method for the analysis of X-ray diffraction line broadening. J Appl Crystallogr 1982;15:308–14. https://doi.org/10.1107/s0021889882012035.

[81] Popa NC. The (hkl) dependence of diffraction-line broadening caused by strain and size for all laue groups in Rietveld refinement. J Appl Crystallogr 1998;31:176–80. https://doi.org/10.1107/S0021889897009795.

[82] Matthies S, Lutterotti L, Wenk HR. Advances in texture analysis from diffraction spectra. J Appl Crystallogr 1997;30:31–42.

[83] International ASTM Standard. E384-Microindentation hardness of materials. Int ASTM Stand 1999;14.

[84] International ASTM Standard. D2845-08: standard test method for laboratory determination of pulse velocities and ultrasonic elastic constants of rock. 2005.

[85] ISO 14317. Sintered metal materials excluding hardmetals — determination of compressive yield strength International Standard. Int Organ Stand 2006;2006:13.

[86] Chang I, Zhao Y. Advances in powder metallurgy: properties, processing and applications. Elsevier; 2013.

[87] Yuan B, Okabe TH. Production of fine tantalum powder by electrochemical method. Mater Trans 2007;48:2687–94. https://doi.org/10.2320/matertrans.M-MRA2007876.

[88] Styrkas AD, Oganyan RA. Production and properties of tin powders produced by ultrasonic atomisation and solid state transformation. Powder Metall 2013;35:117–9. https://doi.org/10.1179/pom.1992.35.2.117.

[89] Ryan G, Pandit A, Ã DPA. Fabrication methods of porous metals for use in orthopaedic applications. Biomaterials 2006;27:2651–70. https://doi.org/10.1016/j.biomaterials.2005.12.002.

[90] Ye B, Dunand DC. Titanium foams produced by solid-state replication of NaCl powders. Mater Sci Eng A 2010;528:691–7. https://doi.org/10.1016/j.msea.2010.09.054.

[91] Wen CE, Yamada Y, Hodgson PD. Fabrication of novel TiZr alloy foams for biomedical applications. Mater Sci Eng, C 2006;26:1439–44. https://doi.org/10.1016/j.msec.2005.08.006.

[92] Nouri A, Hodgson PD, Wen CE. Effect of process control agent on the porous structure and mechanical properties of a biomedical Ti – Sn – Nb alloy produced by powder metallurgy. Acta Biomater 2010;6:1630–9. https://doi.org/10.1016/j.actbio.2009.10.005.

[93] Jha N, Mondal DP, Majumdar JD, Badkul A, Jha AK, Khare AK. Highly porous open cell Ti-foam using NaCl as temporary space holder through powder metallurgy route. Mater Des 2013;47:810–9. https://doi.org/10.1016/j.matdes.2013.01.005.

[94] Xiang C, Zhang Y, Li Z, Zhang H, Huang Y. Procedia Engineering Preparation and compressive behavior of porous titanium prepared by space holder sintering process. 2012. https://doi.org/10.1016/j.proeng.2011.12.518.

[95] German RM. Powder metallurgy & particulate materials processing. 2005. p. 161–72.

[96] Aguilar C, Aguirre T, Martínez C, De Barbieri F, Martín FS, Salinas V, et al. Improving the mechanical strength of ternary beta titanium alloy (Ti-Ta-Sn) foams , using a bimodal microstructure. Mater Des 2020;195:108945. https://doi.org/10.1016/j.matdes.2020.108945.

[97] Shahzeydi MH, Parvanian AM, Panjepour M. The distribution and mechanism of pore formation in copper foams fabricated by Lost Carbonate Sintering method. Mater Char 2016;111:21–30. https://doi.org/10.1016/j.matchar.2015.11.010.

[98] Seul D, Hun C, Hyun S, Yong D, Won J, Woo C, et al. Analysis of cold compaction for Fe-C , Fe-C-Cu powder design based on constitutive relation and artificial neural networks. Powder Technol 2019;353:330–44. https://doi.org/10.1016/j.powtec.2019.05.042.

[99] Balluffi RW, Allen SM, Carter WC. Kinetics of materials. First. Wiley-Interscience; 2005.

[100] Goi KLS, Butler DL, Jarfors AEW, Yong JMS, Lim DCS. Elastic modulus of sintered porous Ti – Si – Zr , using activation by Ti – Si mechanically alloyed powder and TiH_2 powder. Mater Sci Eng A 2008;475:45–51. https://doi.org/10.1016/j.msea.2007.02.129.

[101] S. Sauceda, S. Lascano, B. Luis, G.O. Neves, E. Chicardi, C. Salvo, C. Aguilar, Study of the E ff ect of the floating die compaction on mechanical properties of titanium foams, (n.d.) 1–17.

[102] Salvo C, Aguilar C, Guzmán D, Alfonso I, Mangalaraja RV. Mechanically enhanced novel Ti-based alloy foams obtained by hot pressing. Mater Sci Eng A 2019;759:112–23. https://doi.org/10.1016/j.msea.2019.05.022.

[103] Abhash A, Singh P, Ch VAN, Sathaiah S, Kumar R, Gupta GK, et al. Study of newly developed Ti–Al–Co alloys foams for bioimplant application. Mater Sci Eng A 2020;774:138910. https://doi.org/10.1016/j.msea.2020.138910.

[104] Li Y, Yang C, Zhao H, Qu S, Li X, Li Y. New developments of ti-based alloys for biomedical applications. Materials (Basel) 2014;7:1709–800. https://doi.org/10.3390/ma7031709.

[105] Salvo C, Guzmán D, Alfonso I, V Mangalaraja R. Mechanically enhanced novel Ti-based alloy foams obtained by hot pressing. Mater Sci Eng A 2019;759:112–23. https://doi.org/10.1016/j.msea.2019.05.022.

[106] Ashby MF, Evans T, Fleck NA, Hutchinson JW, Wadley HNG, Gibson LJ. Metal foams: a design guide. 2000.

[107] Nieh TG, Higashi K, Wadsworth J. Effect of cell morphology on the compressive properties of open-cell aluminum foams. Mater Sci Eng A 2000;283:105–10.

[108] Singh P, Singh IB, Mondal DP. A comparative study on compressive deformation and corrosion behaviour of heat treated Ti4wt % Al foam of different porosity made of milled and unmilled powders. Mater Sci Eng, C 2019;98:918–29. https://doi.org/10.1016/j.msec.2019.01.054.

[109] Martínez C, Guerra C, Silva D, Cubillos M, Briones F, Muñoz L, et al. Effect of porosity on mechanical and electrochemical properties of Ti e 6Al e 4V alloy. Electrochim Acta 2020;338:2–11. https://doi.org/10.1016/j.electacta.2020.135858.

[110] Chen SY, Kuo CN, Su YL, Huang JC, Wu YC, Lin YH, et al. Microstructure and fracture properties of open-cell porous Ti-6Al-4V with high porosity fabricated by electron beam melting. Mater Char 2018;138:255–62. https://doi.org/10.1016/j.matchar.2018.02.016.

[111] Kiedrowski MR, Horswill AR. New approaches for treating staphylococcal biofilm infections. Ann N Y Acad Sci 2011;1241:104–21. https://doi.org/10.1111/j.1749-6632.2011.06281.x.

[112] Noor S, Khan RU, Ahmad J. Understanding diabetic foot infection and its management. Diabetes Metab Syndr Clin Res Rev 2017;11:149–56. https://doi.org/10.1016/j.dsx.2016.06.023.

[113] Lugovskoy S, Weiss D, Tsadok U, Lugovskoy A. Morphology and antimicrobial properties of hydroxyapatite–titanium oxide layers on the surface of Ti–6Al–4V alloy. Surf Coating Technol 2016;301:80–4. https://doi.org/10.1016/j.surfcoat.2015.11.050.

[114] Lin N, Huang X, Zou J, Zhang X, Qin L, Fan A, et al. Effects of plasma nitriding and multiple arc ion plating TiN coating on bacterial adhesion of commercial pure titanium via in vitro investigations. Surf Coating Technol 2012;209:212–5. https://doi.org/10.1016/j.surfcoat.2012.07.046.

[115] Whitehead KA, Li H, Kelly PJ, Verran J. The antimicrobial properties of titanium nitride/silver nanocomposite coatings. J Adhes Sci Technol 2011;25:2299–315. https://doi.org/10.1163/016942411X574970.

[116] Bagherifard S, Hickey DJ, de Luca AC, Malheiro VN, Markaki AE, Guagliano M, et al. The influence of nanostructured features on bacterial adhesion and bone cell functions on severely shot peened 316L stainless steel. Biomaterials 2015;73:185–97. https://doi.org/10.1016/j.biomaterials.2015.09.019.